
ASTERIX: MODULE FOR MODELLING THE WATER FLOW ON VEGETATED HILLSLOPES

A PREPRINT

Stelian Ion^{*1}, Dorin Marinescu^{†1}, and Stefan-Gicu Cruceanu^{‡1,2}

¹“Gheorghe Mihoc-Caius Iacob” Institute of Mathematical Statistics and Applied Mathematics of the ROMANIAN ACADEMY, Calea 13 Septembrie No. 13, PO Box 1-24, 050711 Bucharest, Romania

²Corresponding author

January 24, 2025

ABSTRACT

The paper presents an open source software for numerical integration of an extended Saint-Venant model used as a mathematical tool to simulate the water flow from laboratory up to large-scale spatial domains applying physically-based principles of fluid mechanics. Many in-situ observations have shown that vegetation plays a key role in controlling the hydrological flux at catchment scale. In case of heavy rains, the infiltration and interception processes cease quickly, the remaining rainfall gives rise to the Hortonian overland flow and the flash flood is thus initiated. In this context, we also address the following problem: how do the gradient of soil surface and the vegetation influence the water dynamics in the Hortonian flow? The mathematical model and ASTERIX were kept as simple as possible in order to be accessible to a wide range of stakeholders interested in understanding the complex processes behind the water flow on hillslopes covered by plants.

Keywords: Saint-Venant model · porosity · hexagonal raster · numerical scheme · hydrographic basin · C programming · open source

MSC2020: 35-04, 76-04 (Primary); 76-10, 35Q35, 74F10, 65M08 (Secondary)

ACM: G.1.8; G.4

Software availability

Name of software: ASTERIX - Water Flow Module

Developers: Stelian Ion, Dorin Marinescu, Stefan G. Cruceanu.

Email: stefan.cruceanu@ismma.ro

Year first available: 2024.

Program Language: C.

Software Requirements: 32 or 64 bit Linux operating system, gcc compiler, SDL libraries.

Cost: free under [GNU license](#)

Program size: 5 MB.

Availability: http://www.ima.ro/software/ASTERIX_flow_2D.tar.xz

Abbreviations: PDE, Partial Differential Equation; ODE, Ordinary Differential Equation; FVM, Finite Volume Method; SDL, Simple DirectMedia Layer; GPL, GNU General Public License; GIS, Geographic Information System.

*ro_diff@yahoo.com

†marinescu.dorin@ismma.ro

‡stefan.cruceanu@ismma.ro

1 Introduction

Water is an essential element for life on earth, for plants, animals, human beings. Our daily comfort depends on water resources and our way of life is mainly shaped by them, too. The list of disasters over the past 50 years is dominated by the water-related ones which account for 70% of all deaths caused by natural catastrophes [1]. Climate change is affecting the hydrological cycle and increasing the frequency and intensity of the storms. Over 90% of disasters are weather-related, including drought and aridification, wildfire, pollution and floods [2]. Fig. 1 illustrates a report regarding the water-related and non-water-related disasters in OECD countries [3]. Given all that, it is mandatory for

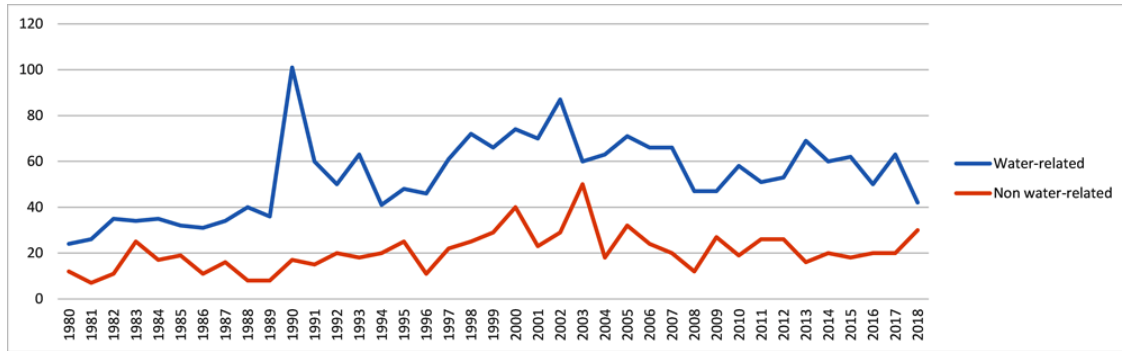


Figure 1: Number of water-related and non-water-related disasters in OECD countries. Source: EM-DAT; The OFDA/CRED International Disaster Database, - Université catholique de Louvain (UCL) - CRED, Debarati Guha-Sapir - www.emdat.be, Brussels, Belgium.

all of us to understand the hydrological cycles to properly manage the water resources in order to protect our life and material well-being.

The water distribution in a hydrographic basin is strongly influenced by many factors related to land cover, land use, soil type or soil surface gradients, [4, 5]. Some of these factors play a key role in controlling the destructive effects of the water-related natural hazards. Mathematical modelling of the hydrological processes is an effective way to estimate the risks associated to these hazards. By modelling, one can make scenarios, can evaluate the level of the risk exposure, and can provide important information regarding an economical water use (e.g. to agronomists).

Modelling the hydrological phenomenon is a very challenging and difficult task with high complexity coming from the various processes involved in: surface runoff, soil erosion, precipitation, infiltration, evaporation, plant transpiration, root uptake, etc., see Fig. 2. We can add the multitude of the factors (only a few being quantifiable) and the environ-

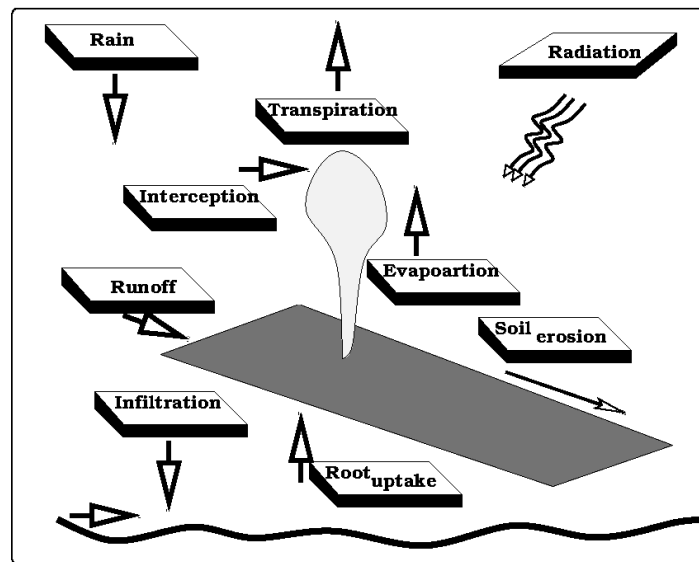


Figure 2: Watershed process

mental heterogeneity (diversity of vegetation and soil, variations in altitude, curvature of the soil surface, etc.) and it becomes obvious that we cannot take everything into account in one single mathematical model. Higher complexity does not guarantee an overall higher performance; the performance can depend on the target purpose or hydrological variables, [6]. Besides this, a complex model often leads to problems of over-parameterization and equifinality [7, 8]. By all means, we do not argue against complex models, we only stress the fact that the modeller must be careful about the processes to be included in the models. *The best models are the ones which give results closest to reality and at the same time require least number of parameters and model complexity*, [9]. We add that a good mathematical model must be *solvable* and *physically relevant*.

The existent models cover a large spectrum of applications: rainfall-runoff, flood hazard management, dam break problems, agricultural hydrology, ecohydrology, and so on. There are many classification criteria of the models and a model can cast into one or more classes, depending on its task, scale or structure. For example, following [9], the models can be classified as metric, conceptual and physics-based ones. Another classification is considered in [10] as empirical, conceptual or physical. The continuous representation of hydrological processes is the main key to a physical model whose equations are based on real hydrological responses. The main advantages of such a model are:

- the spatial and temporal representations of the variables can be accomplished at very fine scales;
- it can be applied to ungauged catchments, provided that one can determine the parameters a priori;
- the effects of a catchment change can be explicitly represented, [9, 10].

In addition, there are many software products that implement mathematical models, some of them are commercial and some others are free. From the last category, we can mention [11, 12, 13] for hydrology-related R and Python tools and resources. Among the most known models in the class of physical models, we mention SHE [14], MIKE-SHE [15], KINEROS [16], VIC [17], PRMS [18], SWASHES [19].

ASTERIX addresses the rainfall-runoff hydrological process using the Saint-Venant equations as a mathematical model. This software is mainly designed to study the combined effects induced by the presence of plant on soil surface and the variation of the gradient of the soil surface on the water dynamics. The plant cover and soil surface are modelled with two space distributed functions: the porosity and the soil altitude. The water-plant stem and water-soil frictional forces are quantified by two functions, both proportional with the square of the water velocity. The coefficients of proportionality are of parameter function type specific to plant cover and soil roughness, respectively. The soil altitude sets the geometrical configuration where the studied processes take place, while the porosity function and the frictional coefficients set the internal structure of this geometrical configuration. The space geometry and the internal structure give rise to the environmental configuration.

The novelty of adding a pointwise distributed porosity function to model the presence of plant cover allows the study of water dynamics for various scenarios with different vegetation distributions.

ASTERIX can be used from a laboratory level up to a hydrographic basin scale. One can use it for practical as well as for theoretical applications, such as:

- problems with water distribution: determination of dry or flooded regions,
- studies on the influence of plants on surface runoffs, estimating their role in the continuum **Soil-Plant-Atmosphere**,
- propagation of floods produced by torrential rains,
- the effects of severe floods due to deforestation,
- studies on Dam Break Problems,
- studies on Riemann Problems, etc.

For practical applications in environmental problems, the numerical approach chosen to solve such porous shallow-water equations must come with a good balance between the computational effort and the accuracy of the obtained solution on one hand, and between the precision of the measured data and the numerical accuracy on the other hand. Although high-order schemes provide better accuracy, they require higher computing effort. Furthermore, using such methods at the scale of hydrographic basins becomes very difficult due to the excessive volume of processed data. These are the reasons we developed and studied in [20] a simple discrete model based on a first-order numerical scheme with low algebraic calculations and reduced memory requirements. This scheme represents the main module of our software ASTERIX for modelling the water flow on vegetated surfaces.

The numerical scheme of the model behind this software was subjected to several internal and external validation tests. Tests such as steady flow over a bump, the oscillating solution of Thacker's Problem, and the solution to the Riemann Problem of the shallow-water equations were used for the internal validation which consists in comparing

the numerical results with the exact solutions of the model. For the external validation, we performed tests to compare the numerical results with laboratory measured data [21, 22]: dam break flow over a bump and in a L-shaped channel, downslope flow through rigid vegetation. A good agreement between the numerical and the exact/measured data was obtained in all these cases. A qualitative analysis emphasizing the similarity between the flow evolution on vegetated soil given by our numerical model and the behavior of the observed phenomenon was also performed to strengthen to confidence in the model.

We mention that the numerical modelling of the water flow in ASTERIX is accomplished on hexagonal rasters due to the cell adjacency and the local symmetry of the hexagonal structure. The advantages of using this type of network are detailed in [23].

This paper is organized as follows: in Section 2 we present the PDE system of the Saint-Venant model with vegetation and the numerical scheme built to approximate this model and implemented in ASTERIX. The software is described in Section 3 and some numerical applications add new examples for additional validation on the method and the software used in Section 4. The last section presents final remarks and conclusions.

2 Mathematical model and numerical scheme

The water flow module of ASTERIX implements a numerical scheme to approximate the Saint-Venant equations with porosity. In order to better understand this software, we briefly present the key concepts concerning the mathematical model and numerical solutions in what follows. The reader is referred to [20] for more details.

2.1 Mathematical model

The Saint-Venant model with porosity we consider in this paper is based on mass and momentum balance equations and takes into account the variation of the soil surface, the plant cover, and the rain as water source. It reads as

$$\begin{aligned} \partial_t(\theta h) + \partial_1(\theta h v_1) + \partial_2(\theta h v_2) &= \mathfrak{M}, \\ \partial_t(\theta h v_a) + \partial_1(\theta h v_a v_1) + \partial_2(\theta h v_a v_2) + \theta h \partial_a w &= \mathfrak{t}_a^p + \mathfrak{t}_a^s, \quad a = 1, 2, \end{aligned} \quad (1)$$

The unknown variables of this PDE system are the water depth $h(t, \mathbf{x})$ and the two components $v_1(t, \mathbf{x})$ and $v_2(t, \mathbf{x})$ of the velocity $\mathbf{v} = (v_1, v_2)$. The external data and forcing functions of this model are:

(a) The altitude of the soil surface

$$x^3 = z(\mathbf{x}), \quad \mathbf{x} = (x^1, x^2) \in \Omega, \quad (2)$$

where $\Omega \subset \mathbb{R}^2$ represents the horizontal projection of the soil surface and is assumed to be a connected bounded open set, x^1 and x^2 are the coordinates along two orthogonal horizontal axes, and x^3 is the coordinate along the vertical axis.

(b) The porosity function

$$\theta : \Omega \rightarrow [0, 1]. \quad (3)$$

This function takes into account the presence of the cover plant on the soil surface and is defined as the volume of void space between the plant stems (volume which can be filled with water) present in a unit volume. We note that $\theta = 1$ for bare soil and $\theta = 0$ for a complete sealant plant cover.

(c) The water source.

The free term \mathfrak{M} quantifies the contribution of rain and infiltration to the water mass balance equation.

(d) The gravitational force.

Its action is quantified through

$$w = g [z(\mathbf{x}) + h], \quad (4)$$

where g represents the gravitational acceleration and $z(\mathbf{x}) + h$ is the free water surface level.

(e) The water-soil frictional forces [24] are quantified by

$$\mathfrak{t}_a^s = -\theta \alpha_s(h) |\mathbf{v}| v_a, \quad (5)$$

where $\alpha_s(h)$ is a non-negative function depending on the given soil surface. Experimental relations of Manning, Chézy, or the Darcy-Weisbach are some of the most used formulas for this coefficient in literature. The Darcy-Weisbach expression

$$\mathfrak{t}_a^s = -\theta \alpha_s |\mathbf{v}| v_a, \quad (\text{Darcy} - \text{Weisbach}), \quad (6)$$

has the advantage of being non-singular if the water depth becomes zero.

(f) The resistance opposed by plants to the water flow [25, 26] is quantified by

$$\mathfrak{t}_a^p = -\alpha_p h (1 - \theta) |\mathbf{v}| v_a, \quad (7)$$

where α_p is a non-negative constant depending on the type of vegetation.

The cumulative effects of the water-soil and water-plants interactions is assumed to be additive in this model, and one can thus introduce the resistance term

$$\mathfrak{t}_a^p + \mathfrak{t}_a^s := -\mathcal{K}(h, \theta) |\mathbf{v}| v_a, \quad (8)$$

where

$$\mathcal{K}(h, \theta) = \alpha_p h (1 - \theta) + \theta \alpha_s(h) \quad (9)$$

is the coefficient function of the frictional force of the water-soil-plant system.

Remark 1. *The Saint-Venant model (1) with porosity addresses the water flow on vegetated surfaces. The structure of the plant cover allows one to use spatial averaging methods, like in theory of flow transport in porous media, see [27] for example. In our case, the “pore space” is the interspace between the plant stems. Urban runoff is another important domain where water flows through obstacles, in this case the “pore space” being the space between buildings.*

Apparently, the two domains are similar, but the structure of the pores is very different. This structural difference imposes different mathematical models, and a model performing well in one case may be inadequate for the other case.

There is a very rich literature devoted to the subject of urban runoff, see [28] for a review of models in this area. We bring also to the reader’s attention the works [29, 30, 31, 32] where one can find very important ideas and facts concerning the urban surface water flow models.

2.2 Numerical scheme

The numerical scheme introduced in [20] to approximate the solution of model (1) casts into the general class of method of lines. We firstly construct a discretization of the spatial variables and differential operators only, and leave the time variable continuous. Then, we define a time discretization scheme to integrate the ODE system previously obtained. A first-order FVM is used for the spatial discretization and a fractional step method for the time discretization [33, 34].

The FVM method has three main ingredients:

- (a) the net of the finite volume elements or the cells decomposition of the fluid flow domain Ω ,
- (b) the cell discretization of the variables (unknowns or external data),
- (c) the approximation of the gradient of the unknown functions on the interfaces of two neighboring cells.

(a) Cell decomposition.

Let $\{\omega_i\}_{i=1, \overline{N}}$ be an admissible polygonal partition [35] of Ω ,

$$\Omega = \bigcup_{i=1}^N \omega_i, \quad (10)$$

with σ_i being the area of the cell ω_i . For any given cell ω_i , we denote

- $\mathcal{N}(i)$ to be the set of all cell-indexes j for which the cell ω_j has a common side (i, j) with ω_i ,
- $\mathbf{n} = (n_1, n_2)^T$ to be the unit normal vector pointing towards the outside of the boundary $\partial\omega_i$ of ω_i .

(b) Cell discretization of the variables.

Any function ψ on a cell ω_i is approximated by a constant value:

$$\psi_i = \psi(\mathbf{x})|_{\mathbf{x} \in \omega_i}. \quad (11)$$

(c) Interface approximations.

For any common interface (i, j) between the cells ω_i and ω_j , we define the following approximations:

$$\theta h_{(i,j)} := \begin{cases} \theta_i h_i, & \text{if } (v_n)_{(i,j)} > 0, \\ \theta_j h_j, & \text{if } (v_n)_{(i,j)} < 0, \end{cases} \quad (12)$$

$$\widehat{\theta}h_{(i,j)} := \begin{cases} \theta h_{(i,j)}, & \text{if } (v_n)_{(i,j)} \neq 0, \\ \theta_i h_i, & \text{if } (v_n)_{(i,j)} = 0 \text{ and } w_i > w_j, \\ \theta_j h_j, & \text{if } (v_n)_{(i,j)} = 0 \text{ and } w_i \leq w_j, \end{cases} \quad (13)$$

and

$$\begin{aligned} (v_a)_{(i,j)} &:= \frac{v_{ai} + v_{aj}}{2}, \quad a = 1, 2, \\ (v_n)_{(i,j)} &:= \mathbf{v}_{(i,j)} \cdot \mathbf{n}_{(i,j)}, \end{aligned} \quad (14)$$

with $\mathbf{n}_{(i,j)}$ denoting the unitary normal to the common side of ω_i and ω_j pointing towards ω_j .

Given the particular (flux conservative - partial) form of (1), we now introduce the following discrete operators:

$$\begin{aligned} \mathcal{J}_{ai}(h, \mathbf{v}) &:= - \sum_{j \in \mathcal{N}(i)} l_{(i,j)} \theta h_{(i,j)} (v_a)_{(i,j)} (v_n)_{(i,j)}, \\ \mathcal{S}_{ai}(h, w) &:= - \frac{1}{2} \sum_{j \in \mathcal{N}(i)} l_{(i,j)} (w_j - w_i) \widehat{\theta}h_{(i,j)} n_a |_{(i,j)}, \\ \mathcal{L}_i((h, \mathbf{v})) &:= - \sum_{j \in \mathcal{N}(i)} l_{(i,j)} \theta h_{(i,j)} (v_n)_{(i,j)}, \end{aligned} \quad (15)$$

where $l_{(i,j)}$ is the length of the common interface (i, j) between the cells ω_i and ω_j . \mathcal{S}_{ai} refers to the gradient of the free water surface, while \mathcal{J}_{ai} and \mathcal{L}_i refer to the flux of the linear momentum and mass, respectively. Combining the spatial discretization with the time fractional step method gives the full discrete scheme associated to (1) of the form

$$\begin{aligned} \sigma_i(\theta_i h_i)^{n+1} &= \sigma_i(\theta_i h_i)^n + \Delta t_n \mathcal{L}_i((h, \mathbf{v})^n) + \sigma_i \Delta t_n \mathfrak{M}_i(t^{n+1}, h^{n+1}), \\ \sigma_i(\theta_i h_i v_{ai})^{n+1} &= \sigma_i(\theta_i h_i v_{ai})^n + \Delta t_n (\mathcal{J}_{ai}((h, \mathbf{v})^n) + \mathcal{S}_{ai}((h, w)^n)) - \Delta t_n \sigma_i \mathcal{K}_i(h^{n+1}) |\mathbf{v}_i^{n+1}| v_{ai}^{n+1}, \quad a = 1, 2, \end{aligned} \quad (16)$$

where a generic ψ_i represents the value of ψ on ω_i for $i \in \overline{1, N}$, φ^n is the value of φ at the moment of time t^n , $\Delta t_n := t^{n+1} - t^n$ is the time step, $|\cdot|$ is the euclidean norm, and

$$\mathfrak{M}_i(t, h) := \mathfrak{M}(t, h_i), \quad \mathcal{K}_i(h) := \mathcal{K}(h_i, \theta_i). \quad (17)$$

To advance a time step, one must solve the system (16) for each cell ω_i , which basically reduces to determining the water depth h_i^{n+1} and velocity \mathbf{v}_i^{n+1} at the time t^{n+1} based on the known values h_i^n , \mathbf{v}_i^n , t^n and Δt_n . The reader is referred to Appendix A for extended details on solving (16) and for details about the restrictions on the time step Δt_n .

3 Software description

ASTERIX is a software developed in C on a Linux operating system, being dedicated to the simulation of water flow on vegetated slopes. It is based on the previously described numerical scheme for the mathematical model (1) and uses a regular hexagonal network for the spatial discretization. SDL libraries are required for visualizing the time distribution of water layer depth or velocities. ASTERIX is distributed under GPL free software license: <https://www.gnu.org/licenses/gpl-3.0.en.html>.

The source code of ASTERIX is a collection of files, most of them containing many specific functions. These component functions can be logically grouped into three categories: Data In, Running and Data Out. One can improve the performance or add new actions by modifying the existent functions or adding new ones. These categories are associated to the three steps of the workflow (see Fig. 3) for operating the software: i) pre-processing, ii) numerical solution, iii) post-processing, respectively. These three steps are relatively independent, depending on the final purposes. The first step is totally independent from the others. The second step depends on the output of the first step, but the simulation can be redone by modifying only some parameters specific to the numerical scheme (e.g maximal time step, final time, etc). The post-processing step depends on the output of the second step. These output data can be also processed by other software. We believe the source code and the accompanying User Guide contain sufficient details to allow a C advised programmer to make the desired modifications.

Data In.

The functions in this category collect the external information and set values to the internal variables and to the hyper-parameters of the program. The most important work is to process the environmental data concerning the soil altitude, plant cover density, and plant and soil characteristic parameters related to the frictional forces.

Domain geometry and the cell partition of the flow domain. The topographic information of the soil provided by a GIS raster is ported to a regular hexagonal raster along this step. One edits the file `hexa_parameters.dat` in order to establish the number of hexagonal cells on the first row of the hexagonal grid. The number of lines of the hexagonal raster is then automatically calculated depending on the geometry of the GIS raster.

Note: The program also allows the option to work on a rectangular subdomain cut from the GIS raster.

The executable “convert” generates data files with information on the hexagonal raster (e.g. cell radius, cell centers, cell elevations, cell neighbors, cell interfaces, cell types⁴, etc.) that are required by the main program for flow simulation. Details about the mathematical framework for porting data methods can be found in [23].

One can also artificially create the topography of a soil using some mathematical functions. In this case, the topographic information data can be directly generated on a regular hexagonal raster using the executable “generate”.

Boundary conditions. The boundary conditions are themselves a rather difficult challenge due to the hyperbolic type of the system of equations. Furthermore, identifying the parts of the border on which different conditions must be established represents another difficulty. The software allows various boundary conditions as free discharge, given mass flux, impermeable wall, and Dirichlet. Depending on the studied problem, ASTERIX allows combinations of such boundary conditions as can be seen on the various tests considered in Section 4. We point out that default boundary condition is free discharge; for other types of boundary conditions, the user must define the configuration of the boundary with the specific boundary conditions for the problem one has to solve. In principle, the software allows spatial and time-varying boundary conditions, but such facilities are not yet implemented at this stage; they must be hard-coded by the user.

Parameters. The flow simulation program can be controlled through a series of parameters whose values can be modified in the “parameter_control.dat”, file such as:

1. *environmental parameters*
 - (a) water-soil friction coefficient;
 - (b) water-plant friction coefficient;
 - (c) plant density;
2. *program hyper-parameters*
 - (a) total running time;
 - (b) maximum time step;
 - (c) the type of representation;
 - (d) choosing an initial water layer or using one rain simulator;
 - (e) extraction of snapshots at different moments of time;
 - (f) control of color shades for representations;
 - (g) the output data files we want to get at the end.

Running.

The flow is simulated via the executable “2D_flow” on the regular hexagonal grid. The program can be run with or without graphical representation. The option *without graphics* shortens the runtime for finding the numerical output.

Data Out.

The program is able to generate files with numerical data for certain quantities of interest at different moments of time. In particular, one can generate data files with the evolution of the water depth and velocities at certain predetermined points on the terrain.

When run *with graphics*, the program allows three graphical representations:

1. the relief only;
2. the evolution of the water depth distribution;
3. the evolution of the water velocity field.

⁴In terms of belonging to the domain Ω , the hexagonal raster of the soil surface contains internal cells and boundary cells, corresponding to the interior and boundary parts of Ω , respectively.

If the option “relief only” is selected, ASTERIX allows the user to inspect the terrain in order to find some information about the hexagonal cells of the raster as the coordinates of their centers, the altitudes, etc. This information can be useful when one desires to establish monitoring points.

Our software includes the GIS files of some hydrographic basins with the help of which one can quickly test how the software works on real topographies. One can easily add new GIS data files for simulations on other topographies. The software has also several analytic functions implemented for simulating the flow for theoretical or laboratory experiments. The user with some experience in C can add new functions in the available sources.

The directory structure and the operating diagram of ASTERIX are synthesized in Table 1 and Fig. 3, respectively. Extended details can be found inside the User Guide.

Table 1: Folder structure of ASTERIX with the key files

Folder	Content	Description
GIS	.asc	DEM files containing the topography of some real terrains (e.g. ampoi, lipaia, paul, susita).
gis_hexa_conversion	.c, .h	The C sources and header files for porting the raster data of a file from GIS into a hexagonal raster.
generate_artificial_gis	.c, .h, .dat	The source code and header files for generating the hexagonal raster of a soil surface defined by a mathematical function in the .dat file.
ini	.dat	Files with input data.
main	.c, .h	The main code files for the flow simulation.
out		A place where the output (.dat, .png) files will be saved.

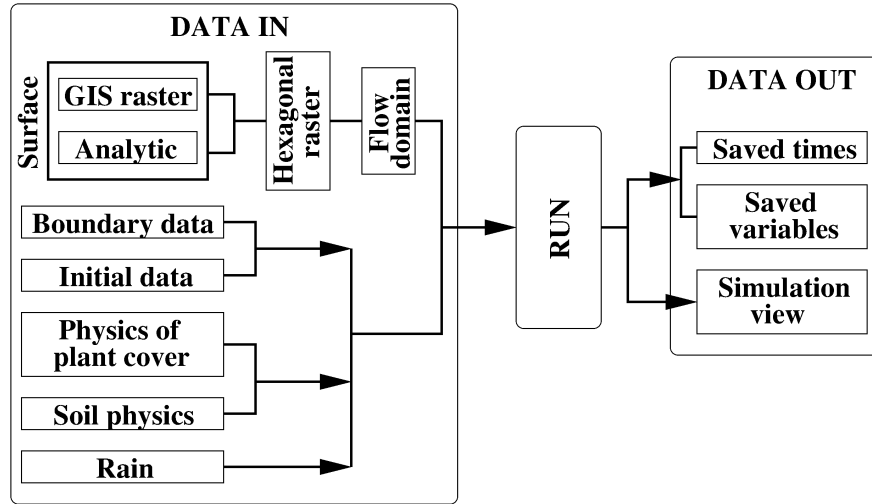


Figure 3: Diagram (sketch) of the ASTERIX software

The variables and the parameters describing model (1) and their encoded names inside the software are also sketched in Table 2.

Table 2: The variables and the main parameters of (1) with (8) and (9), and their encoded names in ASTERIX

	Encoded name in ASTERIX	Var & param.	Refers to
Unknown	water_vector[.]	$h(t, \mathbf{x})$	Water dynamics
	velocities[.][.]	$\mathbf{v}(t, \mathbf{x})$	
External data	elevation_vector[.]	$z(\mathbf{x})$	Soil topography
	theta_veg[.]	$\theta(\mathbf{x})$	Physics of plant cover
	alpha_veg	α_p	Physics of soil
alpha_terr	α_s		

Table 3 presents a list of the main files for running ASTERIX.

Table 3: Main files for running ASTERIX. be - binary executable; bs - Bourne-Again shell script; df - data file

Main Files	Type	Placement	Description
convert	be	gis_hexa_conversion	It converts the data from a DEM file from 'GIS/' into a hexagonal raster and populates 'ini/' with the input .dat files necessary for the main program '2D_flow'.
generate	be	generate_artificial_gis	It generates a hexagonal raster for a particular type of artificial relief selected from field_function_parameters.dat and populates 'ini/' with the input .dat files necessary for the main program '2D_flow'.
2D_flow	be	main	The main executable file for simulating the water flow.
artificial_relief_selection.sh	bs	main	It allows one to select the desired artificial relief from field_function_parameters.dat generates the hexagonal raster through the executable 'generate'.
natural_relief_selection.sh	bs	main	It allows one to select the desired natural relief from 'GIS/' and generates the hexagonal raster through the executable 'convert'.
vpha.sh	bs	main	It allows one to choose the resolution of the hexagonal network associated by editing the file 'hexa_parameters.dat' and generates the hexagonal raster through the executable 'generate' for a specific artificial relief.
vphn.sh	bs	main	It allows one to choose the resolution of the hexagonal network by editing the file 'hexa_parameters.dat' and converts the data from a DEM file from 'GIS/' into a hexagonal raster through the executable 'convert' for a specific natural relief.
vpc.sh	bs	main	It allows one to quickly edit the file 'control_parameters.dat' and to modify the data from this file.
no_graphics.sh	bs	main	It creates the folder 'main-no_graphics/' and populates it with the simplified code files (without any graphics) of ASTERIX. The flow simulation with numerical data output only can now be run from this folder.
control_parameters.dat	df	ini	It contains the values of different parameters necessary for running ASTERIX at a given resolution.
hexa_parameters.dat	df	ini/ini_hexa	It contains the values of the parameters for the hexagonal grid resolution.
field_function_parameters.dat	df	generate_artificial_gis	It contains the data for some types of artificial reliefs.
susita.asc	df	GIS	A DEM file with the GIS data for the Susita River basin.
ampoi.asc	df	GIS	A DEM file with the GIS data for the Ampoi's Valley.
lipaia.asc	df	GIS	A DEM file with the GIS data for the Lipaia's Valley.
paul.asc	df	GIS	A DEM file with the GIS data for the Paul's Valley.

Assuming the user has downloaded, decompressed the archive of ASTERIX and compiled the files, we now present a simple example for operating the software on Şuşița River basin described in Subsection 4.2.1.

Go to folder 'main/' and execute the following commands:

```
$ ./natural_relief_selection.sh susita
```

```
$ ./2D_flow
```

The last command runs ASTERIX with a graphic representation of the water depth over time; the user can also run

```
$ ./2D_flow -r2
```

for a graphic representation of velocity field over time. More details on operating the software can be found in the accompanying 'User Guide'.

4 Performance Tests

A suite of examples is presented in [20] for the purpose of validating the numerical scheme. In what follows, we add some new examples for testing the performance of the software. The numerical results are compared with the analytic solutions for some of them and with the laboratory measurements for others. We analyze the response of the software to real terrain data and perform a sensitivity analysis with respect to some model as well as some software parameters.

4.1 Theoretical Tests

4.1.1 Flow on radial symmetric surfaces

A first test was performed on two theoretical surfaces with radial symmetry. These soil surfaces pictured on the first row of Fig. 4 are built using a parametric representation

$$\begin{cases} x^1 = r \cos \theta \\ x^2 = r \sin \theta \\ x^3 = f(r) \end{cases} \quad (18)$$

on an annulus

$$D := \{(r, \theta) \mid r \in [r_0, r_1], \theta \in [0, 2\pi)\},$$

with $r_0 = 10$, $r_1 = 100$, and

$$f(r) = A + s \cdot A \cos\left(\frac{\pi(r - r_0)}{r_1 - r_0}\right), \quad (19)$$

with $A = 10$ m, $s = -1$ for the Crater surface on the left column and $s = +1$ for the Hillock surface on the right column. The boundary conditions are of Dirichlet type for the upper part and free discharge for the bottom part of both surfaces:

$$h(t, \mathbf{x}) = h_0, \quad \mathbf{v}(t, \mathbf{x}) = -v_0 \mathbf{n}, \quad \forall \mathbf{x} \in \partial D^{\text{in}}, \quad (20)$$

where ∂D^{in} is the upper boundary of the surface, \mathbf{n} is the external oriented unit normal vector of ∂D^{in} at \mathbf{x} , and $h_0 = 0.05$ m, $v_0 = 1$ m/s. The advantage of such radial symmetric surfaces is that we can write the analytic solution of the flow in steady state [36].

The numerical solution was obtained with ASTERIX on a hexagonal raster with approximately 900000 cells of radius 0.115 m. A comparison between the analytic and numerical water depth and velocity distributions of the stationary solution of the water flow along a radial section is presented in Fig. 4. For the errors between the two solutions we used the formulas

$$\epsilon_h = \frac{1}{N} \sum_{i=1}^N \left| \frac{h_n(r_i) - h_a(r_i)}{h_a(r_i)} \right|, \quad \epsilon_v = \frac{1}{N} \sum_{i=1}^N \left| \frac{v_n(r_i) - v_a(r_i)}{v_a(r_i)} \right|,$$

where N is the number of points r_i from D at which the numerical solution is evaluated. h_n and h_a stand for the numerical and analytic water depth, respectively. v_n and v_a stand for the numerical and analytic water velocity, respectively.

The small values of the errors presented in Table 4 show there is a good agreement between the analytic and numerical solutions.

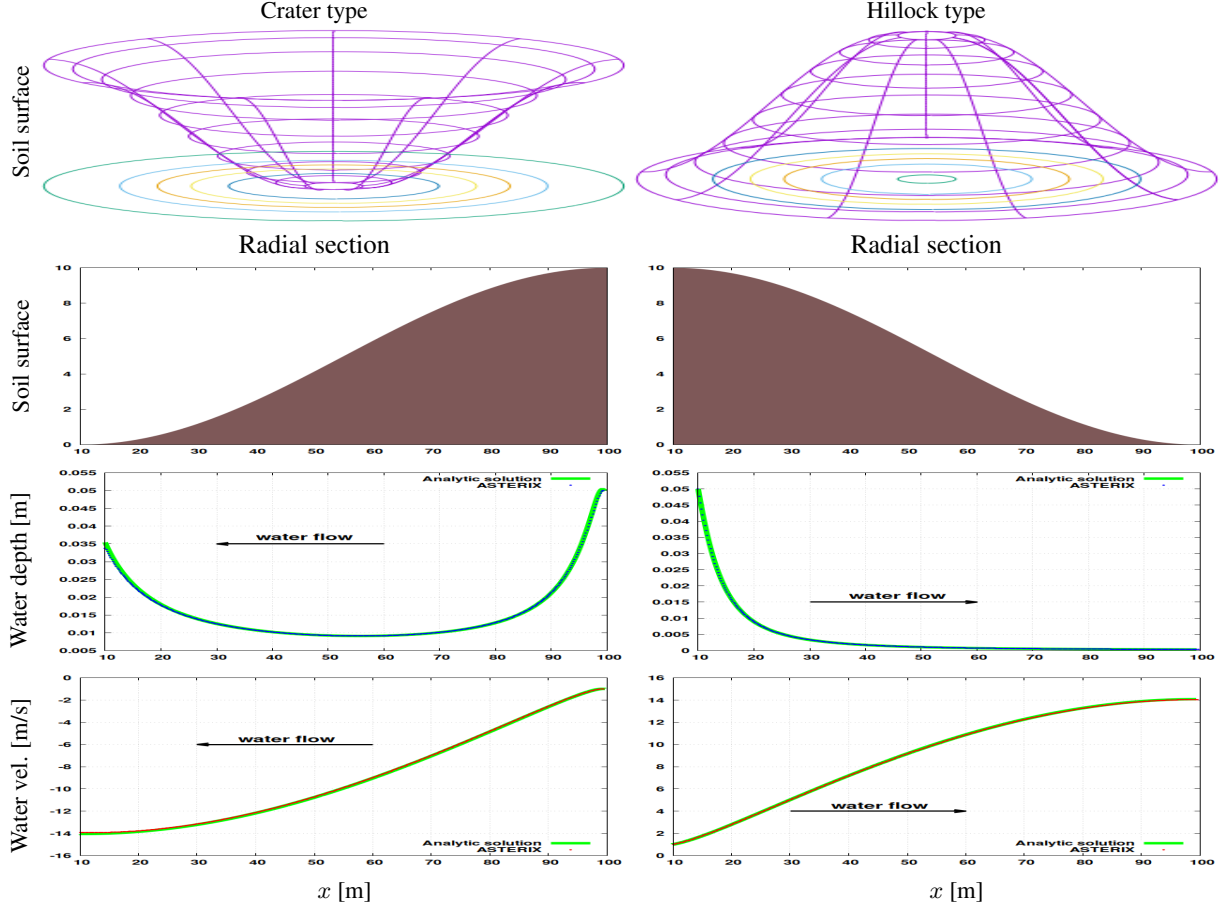


Figure 4: The stationary solution of the water flow on two radial symmetric surfaces: crater type (first column) and hillock type (second column). Boundary conditions: $h = 0.05$ m and $v = 1$ m/s at the top of the surface and free drainage at the bottom.

Table 4: Relative mean error between the numerical and analytic steady state solutions.

	Crater type soil	Hillock type soil
ϵ_h	0.0055	0.0111
ϵ_v	0.0040	0.0018

4.1.2 Thacker's Problem

The next 2D experiment, Thacker's Problem, is a powerful test to check the ability of our software to catch and highlight the propagation of a wet/dry front. The singularity appearing at the wet/dry contact between water and soil surfaces raises difficulties for many numerical methods, but a huge advantage of this problem is that it can be exactly solved [19, 37, 38, 39] and thus, one can make use of its analytic solution to theoretically test the developed numerical method.

Thacker's Problem is basically formulated as the PDE system (1) modelling the flow dynamics over a paraboloid type surface

$$z(x, y) = a(x - x_0)^2 + b(y - y_0)^2, \quad a, b > 0, \quad (21)$$

in the absence of vegetation ($\theta = 1$) and mass source ($\mathfrak{M} = 0$), for a soil resistance term of the form

$$\mathfrak{t}_a^s = -\tau h v_a, \quad a = 1, 2, \quad (22)$$

where τ is a proportionality coefficient, and for a fluid velocity which does not depend on the space variable.

Depending on the values of some parameters, the exact solutions of this problem can be classified into oscillating, non-oscillating and mixed ones. In [20], we have considered the case of Thacker's Problem with an oscillating solu-

tion and compared it with the numerical one described there and implemented in ASTERIX. In this subsection, we present a comparison between a non-oscillating solution for Thacker's Problem and the numerical solution provided by ASTERIX⁵. The non-oscillating solution was obtained using $a = 1.25 \cdot 10^{-3}$, $b = 5 \cdot 10^{-3}$, $x_0 = y_0 = 500$ m in (21), and a proportionality coefficient of the friction force $\tau = 0.7 \text{ s}^{-1}$ in (22). The reader is referred to Appendix B for extended mathematical details about the analytic solution to this problem.

We consider the following initial data:

$$u_0 = v_0 = 0, \quad u'_0 = 0.02g, \quad v'_0 = -0.1g, \quad w_0 = 15 \text{ m}, \quad (23)$$

where $g = 9.81 \text{ m} \cdot \text{s}^{-2}$ is the gravitational acceleration. Fig. 5 shows that our numerical solution (obtained on a regular hexagonal mesh with 487123 cells of radius 0.888231 m) is in accordance with the non-oscillating planar free water surface given by the analytic solution to the Thacker's Problem.

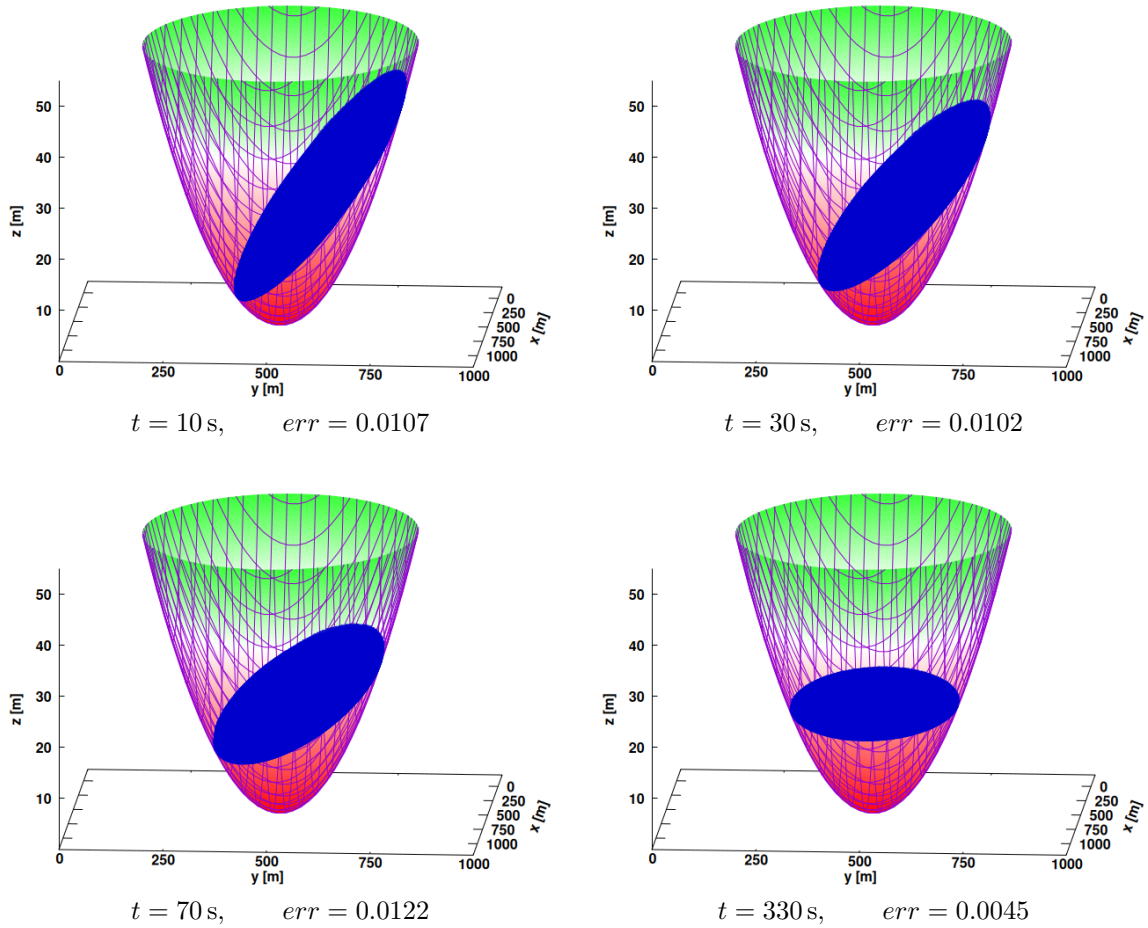


Figure 5: 2D Thacker's Problem: dynamics of the numerical free water surface. These snapshots are obtained using Gnuplot on the data calculated with ASTERIX at four different moments of time: $t = 10, 30, 70, 330$ s. The error err between the numerical and exact values of the free water surface at each of the four moments of time is calculated with $err = \|((h+z)^{app} - (h+z)^{ex})/(h+z)^{ex}\|_{\infty}$.

The evolution of the error

$$err = \|((h+z)^{app} - (h+z)^{ex})/(h+z)^{ex}\|_{\infty}$$

between the exact and numerical solution is pictured in Fig. 6.

Fig. 7 shows a comparison between the time evolution over time of the numerical and analytic solutions of the free water surface at the three different points P_1, P_2, P_3 from Table 5.

⁵The soil resistance term t_a^s is theoretically chosen to be proportional to the water depth and velocity in Thacker's Problem in order to obtain an analytic solution. Note that this form (22) is different from (6), and ASTERIX was modified accordingly.

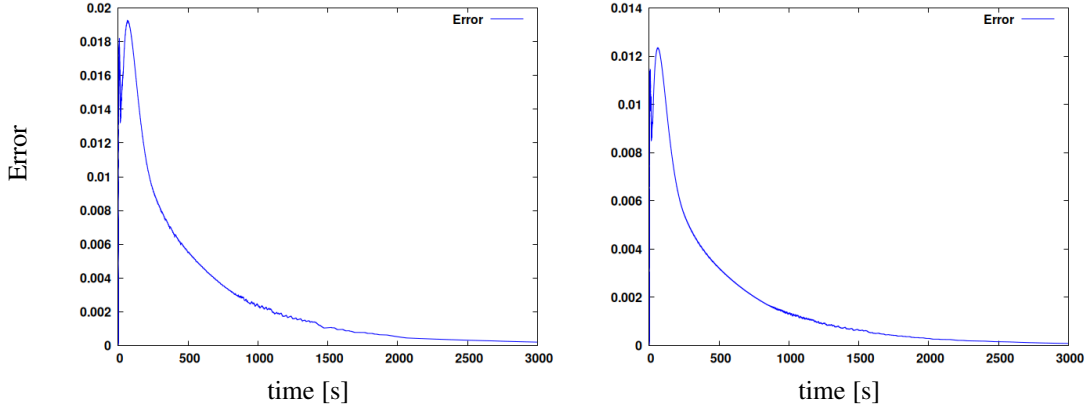


Figure 6: 2D Thacker's Problem: time evolution of the error $err = \|((h+z)^{app} - (h+z)^{ex})/(h+z)^{ex}\|_{\infty}$ between the analytic and numerical solutions on two hexagonal networks with different cell sizes: 1.65 m and 0.888 m for the left and right picture, respectively.

Table 5: Data for the three points in Tacker's Problem where the evolution over time of the free water surface is drawn in Fig. 7.

	P_1	P_2	P_3
x	577.692	500.000	264.615
y	451.221	500.518	564.471
z	1.944	0	9.004

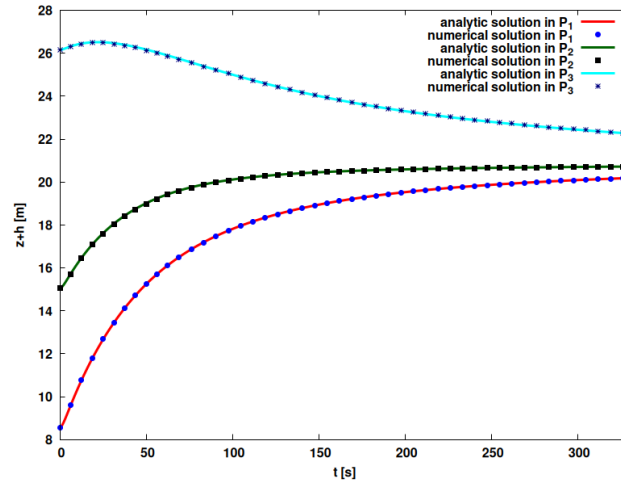


Figure 7: 2D Thacker's Problem: time evolution of the free water surface at the three points from Table 5.

4.1.3 Test on a Riemann Problem with vegetation

Riemann Problem is a mathematical subject associated to the Dam Break Problem, a real physical phenomenon. It represents a very important issue in the theory of hyperbolic systems because one can find an analytical solution of the problem for a broad spectrum of initial data.

The analytic solution is set up by a bunch of very special solutions, namely, shock waves and simple waves. The combination of these waves in a packet is ruled by a physical admissibility criteria. In the absence of such criteria the Riemann Problem can have a multitude of solutions, some of them having no physical sense. A numerical scheme is considered to be at least physically acceptable if it correctly predicts both types of waves.

The existence of the solution and its very special structure make the Riemann Problem almost a mandatory test for any numerical scheme dedicated to the shallow water equation.

The objective of our test is twofold: one aim is to verify how well the numerical solution approximates the true solution of the problem, and the other one is to verify if the 2D numerical scheme furnishes a markedly 1D solution for appropriate initial data and boundary conditions.

In this section, we choose a very difficult problem where both the soil surface and the porosity function exhibit simultaneous jumps. The piecewise constant soil surface and porosity functions

$$(\theta, z)(x, y) = \begin{cases} (\theta_L, z_L), & x \leq 9 \\ (\theta_R, z_R), & x > 9 \end{cases} . \quad (24)$$

are given on a 18 m long and 1 m wide horizontal rectangular channel. The piecewise constant initial data are given by

$$h(x, y)|_{t=0} = \begin{cases} h_L, & x \leq 9 \\ h_R, & x > 9 \end{cases} , \quad (25)$$

$$v(x, y)|_{t=0} = \begin{cases} (u_L, 0), & x \leq 9 \\ (u_R, 0), & x > 9 \end{cases} , \quad (26)$$

whose numerical values are in Table 6.

Table 6: Data for the 2D Riemann Problem

θ_L	z_L	h_L	u_L	θ_R	z_R	h_R	u_R
-	[m]	[m]	[m/s]	-	[m]	[m]	[m/s]
0.8	1.0	0.2	5.00	1.0	1.2	0.6	1.33

The exact solutions of Riemann Problem are difficult to find and have only been studied in the one-dimensional case. For the 2D test considered in this subsection, the problem of finding the solution can be reduced to a 1D case for which it was shown the existence and uniqueness, [40]. The water surface calculated with ASTERIX at $t = 1.5$ s and a comparison between the analytic solution and the numerical data on a longitudinal section are presented in Fig. 8.

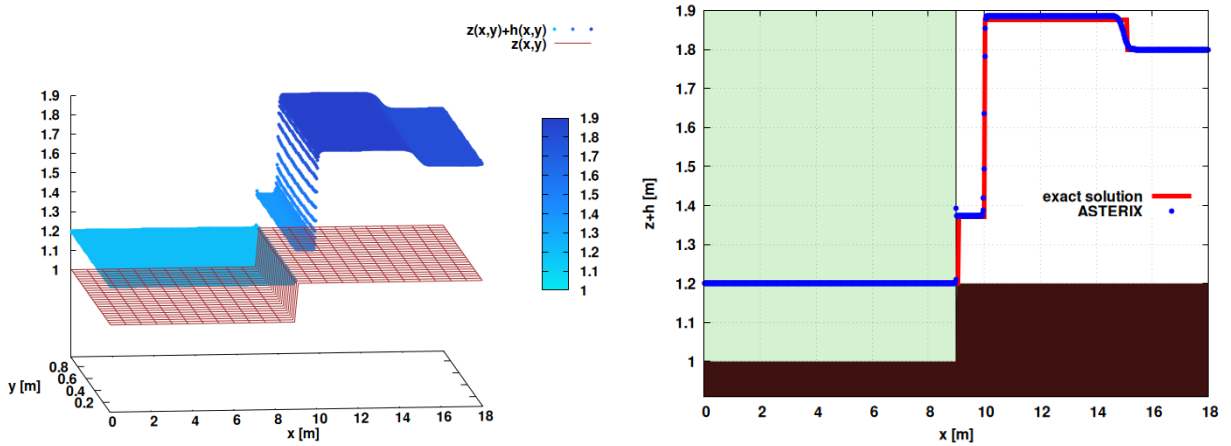


Figure 8: 2D Riemann's Problem: free water surface found with ASTERIX at $t = 1.5$ s (left picture) and a comparison between the analytic and numerical solutions from a longitudinal channel section (right picture, where the vegetated and the bare parts of the soil are marked with green and white, respectively).

The value of the mean relative error

$$\frac{1}{N} \sum_{i=1}^N \left| \frac{(h+z)_i^{app} - (h+z)_i^{ex}}{(h+z)_i^{ex}} \right|$$

between the numerical (*app*) and exact (*ex*) values of the free water surface is 0.003785, where $N = 1122$ is the number hexagonal centers along the longitudinal section.

We remark that the three shock waves developed by the exact solution are also caught by ASTERIX. Furthermore, one can observe that the hexagonal grid used by our software does not induce numerical adverse effects such as additional head losses due to the impossibility of the hexagons to align exactly with the channel walls.

4.2 Tests on real data

4.2.1 Simulation on Șușița River basin with vegetation

Șușița's hydrographic basin is the catchment area of Șușița River in Vrancea County, Romania.

Unfortunately, we do not have data for the water distribution, plant cover density and measured velocity field in a hydrographic basin to compare our numerical results with. However, to be closer to reality, we have used the GIS data for an approximately 370 km^2 soil surface included in a $64 \times 28 \text{ km}^2$ rectangular area. More precisely, this rectangular area, Fig. 9, lies north-west of Tișița whose geographical coordinates are $45^\circ 50' 36''$ North, $27^\circ 13' 32''$ East.

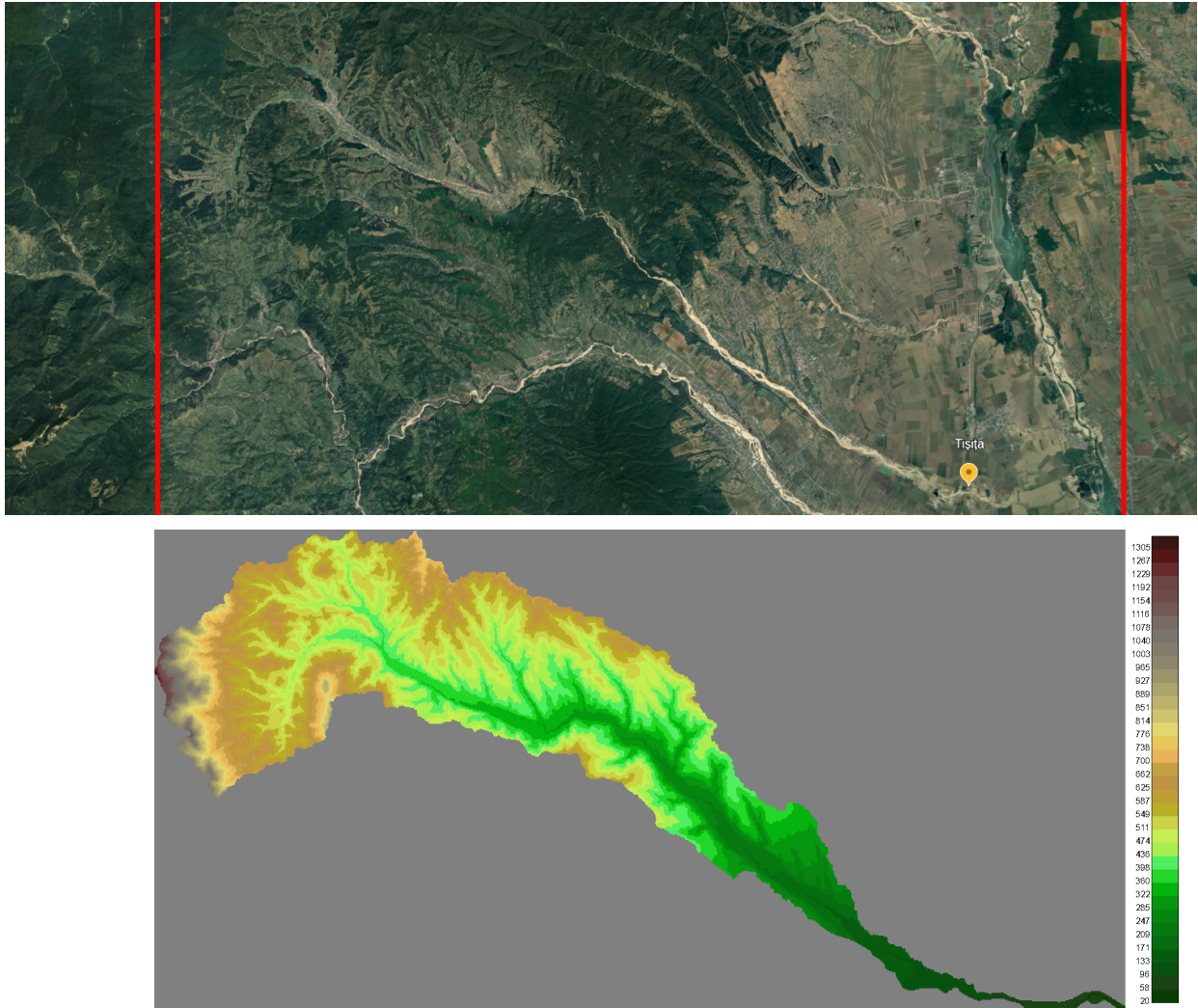


Figure 9: Șușița's hydrographic basin. Satellite image [41] and the terrain reconstructed (from GIS data) on a hexagonal network.

We accomplished a theoretical experiment: starting with a uniform rainfall generated by a triangular model (see Appendix C for extended details) and characterized by

- the total time $T_d = 1000 \text{ s}$ of the rain,
- the maximum intensity $i_a = 0.0732 \text{ mm/s}$ of the rain, and
- the time $t_a = 250 \text{ s}$ at which this maximum intensity is recorded,

on the entire basin and using two different uniform vegetation densities ($\theta_1 = 1.0$ and $\theta_2 = 0.97$), we ran ASTERIX on a network with 82148 internal hexagonal cells of radius 41 m.

The water depth distribution at a given moment in time is comparatively presented in Fig. 10 using a blue color gradient (the darkest blue corresponds to the cells with $\theta h \geq 4h_0$, where $h_0 = i_a * T_d / (2 * 1000) = 0.0366$ m is the rainfall depth). The water velocity distribution at the same moment in time is pictured in Fig. 11 using a red color gradient for the modulus of the velocity and arrows for the flow direction. The convention of coloring the relief where $\theta h \leq 0.1h_0$ is applied for both figures. The data in Table 7 confirms that more water is retained in the basin if the vegetation is denser.

Table 7: Data for the theoretical experiment on Şuşița’s hydrographic basin. ASTERIX was run for $t = 3000$ s.

θ	Rainfall [m ³]	Water out [m ³]	Water left [m ³]
1.00	13166903	104416	13062487
0.97	13166903	90808	13076095

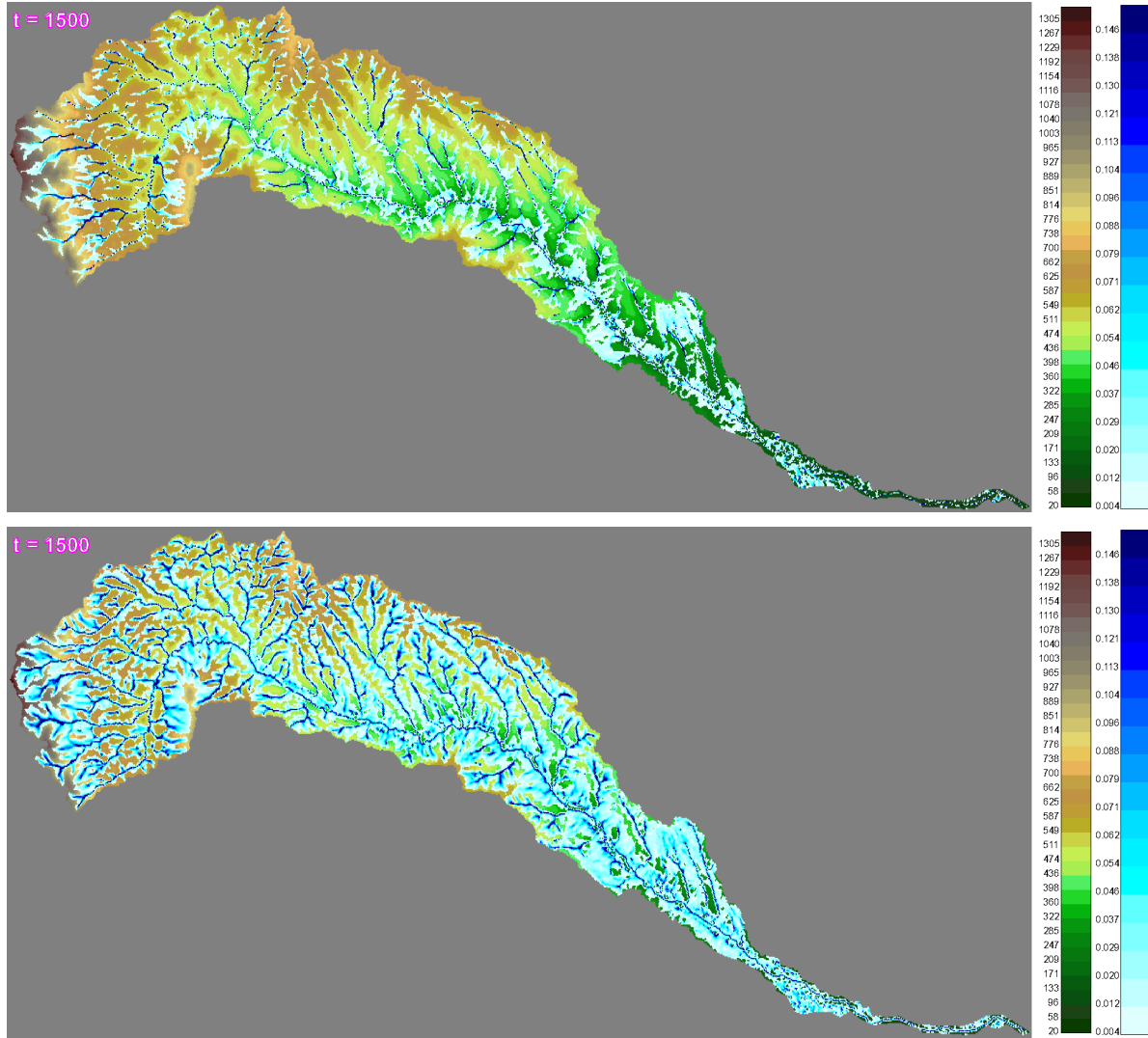


Figure 10: Snapshots of water depth distribution on Şuşița’s hydrographic basin at $t = 1500$ s for two different uniform vegetation densities: $\theta = 1.0$ and $\theta = 0.97$ on the upper and bottom picture, respectively. The first and the second column bar next to the figures are the color palettes used for the relief and water depth, respectively. As expected, our numerical data are consistent with terrain observations: the amount of water leaving the basin is greater in the case of lower vegetation density.

Furthermore, Fig. 12 emphasizes that the maximal discharge rate is smaller and occurs later when vegetation is denser.

Fig. 13 illustrates the amount of water leaving the basin over time for different mesh sizes. One can observe that the curves are getting closer to each other as the grid resolution increases. This suggests a convergence property of the numerical solution to the true solution of the model.

Remark 2. One can easily test ASTERIX (without having to modify the code) for a terrain given by a GIS data file (e.g. susita.asc). Assuming that the source code is already compiled, launch from the 'main' directory

```
$.natural_relief_selection.sh susita
```

```
$.2D_flow
```

The reader is referred to the User Guide for extended details.

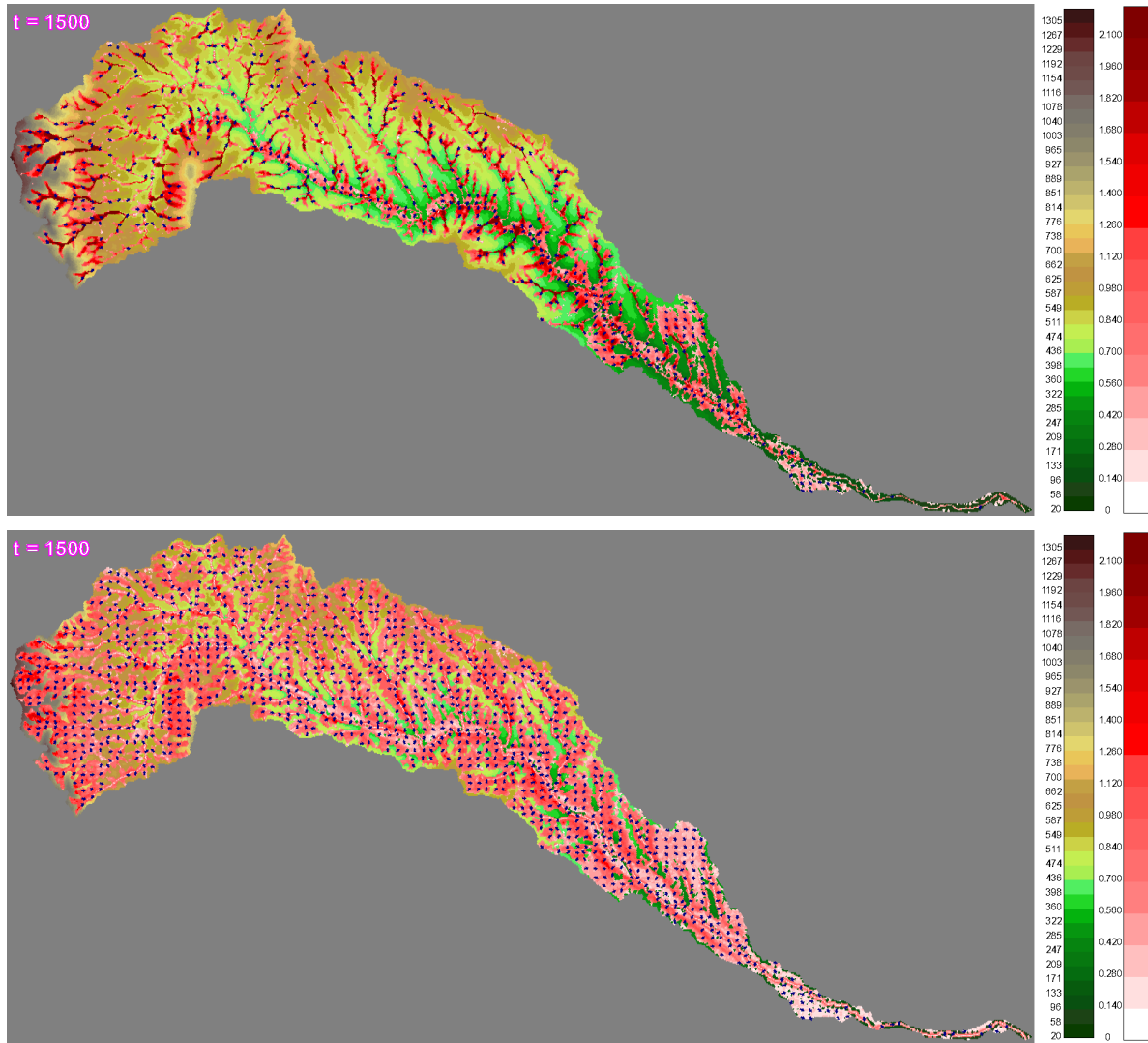


Figure 11: Snapshots of water velocity distribution on Şuşița’s hydrographic basin at $t = 1500$ s for two different uniform vegetation densities: $\theta = 1.0$ and $\theta = 0.97$ on the upper and bottom picture, respectively. The first and the second column bar next to the figures are the color palettes used for the relief and modulus of the water velocity, respectively. As expected, the velocities are smaller when vegetation is denser.

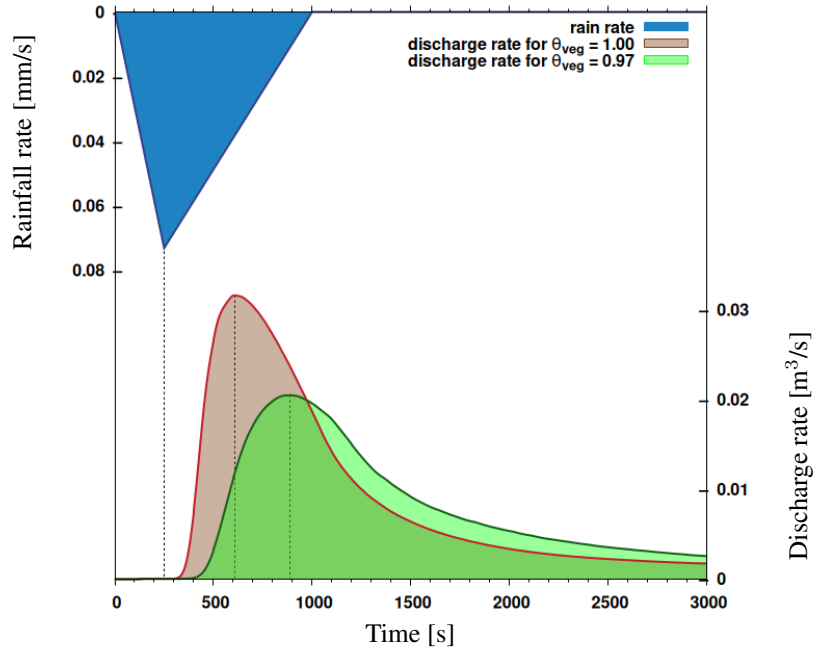


Figure 12: Simulation of a rainfall and the discharge rates on Şuşița's hydrographic basin for two different uniform vegetation densities ($\theta = 0.97$ and $\theta = 1$).

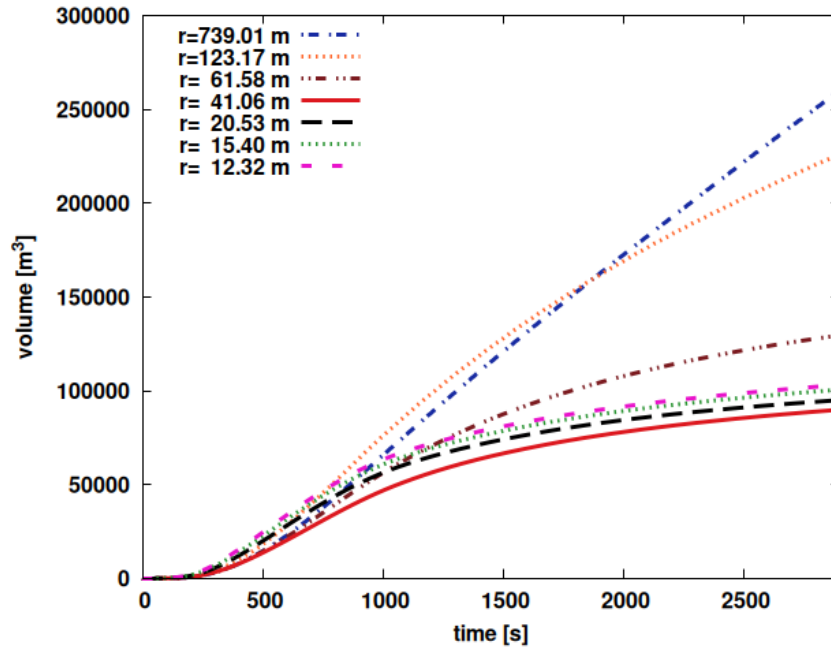


Figure 13: The evolution of the total water leaving the basin over time for different grid resolutions.

4.2.2 Flow over a slope with vegetation

The flow on vegetated areas is more complex than on bare soil, which may explain the limited availability of reported data. In this section, we compare the numerical results provided by ASTERIX with those reported in [22].

The experimental installation consists of a rectangular laboratory flume (18 m long and 1 m wide) with a longitudinal bottom slope $S = 1.05$ mm/m and partially covered with vegetation. The vegetation is modelled using uniformly distributed emergent circular cylinders of radius $R_c = 5$ mm and has a density of $N = 81$ cylinders/m². This type of vegetation allows the estimation of the porosity by $\theta_v = 1 - N\pi R_c^2 \approx 0.99364$. Six experiments were performed for different given values of the upstream flow rate q_L , free downstream discharge, two types of vegetation distribution,

$$\theta_1 = \begin{cases} 1, & x \in [0, 9) \\ \theta_v, & x \in [9, 18] \end{cases}, \quad \theta_2 = \begin{cases} \theta_v, & x \in [0, 9) \\ 1, & x \in [9, 18] \end{cases},$$

and $z = -m(x - 18)$, $x \in [0, 18]$, with $m = 0.105$ mm/m. The values of q_L for the first three experiments where vegetation is present on the lower half of the channel ($\theta = \theta_1$) are

$$q_{11} = 7 \text{ l/s}, \quad q_{21} = 15 \text{ l/s}, \quad q_{31} = 21 \text{ l/s},$$

while the ones for the last three experiments where vegetation is present on the upper half of the channel ($\theta = \theta_2$) are

$$q_{12} = 7 \text{ l/s}, \quad q_{22} = 15 \text{ l/s}, \quad q_{32} = 50 \text{ l/s}.$$

The numerical simulations are carried out using ASTERIX with the following boundary conditions

$$uh(t, 0) = q_L, \quad \partial_x u(t, 18) = \partial_x h(t, 18) = 0,$$

and the following values of the friction parameters

$$\alpha_s = 0.00709 \quad \text{and} \quad \alpha_p = 73.39.$$

A comparison between the measured data and numerical water depth is illustrated in Fig. 14. For each experiment l ,

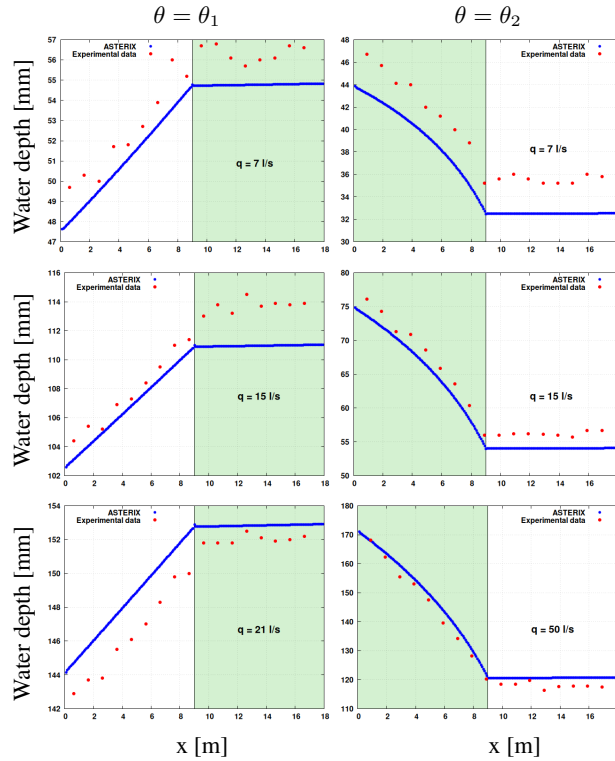


Figure 14: Longitudinal profiles of water depth for the flow over a slope. The vegetated and the bare parts of the soil are marked with green and white, respectively.

the error ϵ (in [mm]) between the two solutions is calculated with

$$\epsilon := \sqrt{\frac{1}{N_g} \sum_{i=1}^{N_g} (h^{\text{exp}}(x_i^l) - h(x_i^l))^2}, \quad l = \overline{1, 6},$$

where $N_g = 17$ is the number of gauges placed inside the channel for measurements, x_i^l is the position of the gauge G_i on the l^{th} experiment, while h^{exp} and h are the measured and calculated water depths of the stationary flow, respectively. Table 8 presents the values of these errors.

Table 8: The errors between the numerical solution and the experimental data pictured in Fig. 14

θ	θ_1			θ_2		
q_L	q_{11}	q_{12}	q_{13}	q_{21}	q_{22}	q_{23}
ϵ [mm]	1.48	2.05	1.73	3.08	2.10	2.73

Fig. 15 illustrates the water depth and the velocity field on the entire channel for the last experiment from Table 8 where $\theta = \theta_2$ and $q_L = q_{23}$. The water depth presented here corresponds to the longitudinal profile found on the third row and second column in Fig. 14. One can observe that the water depth (and velocity) longitudinal profile is the

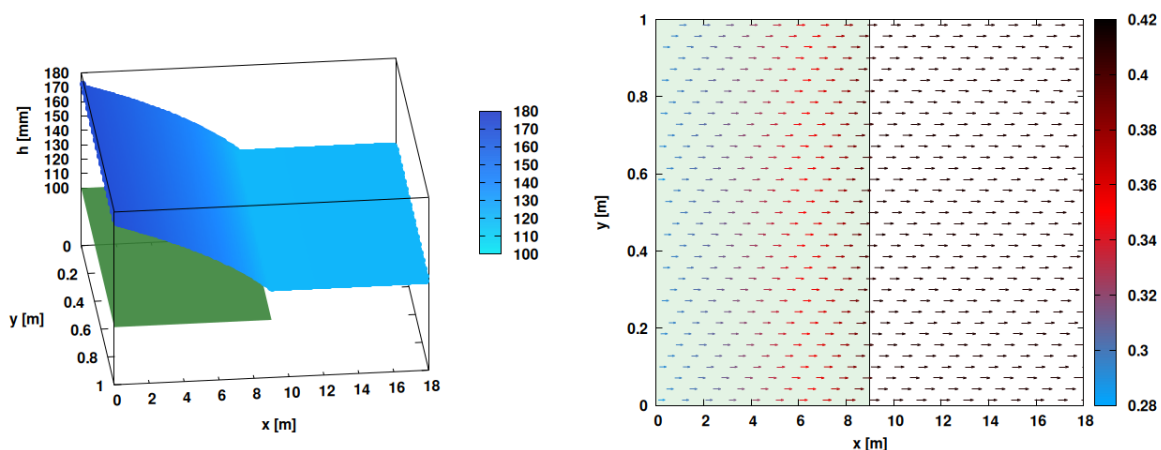


Figure 15: Flow over a slope with vegetation: water depth [mm] and velocity field [m/s] obtained with ASTERIX for the sixth experiment where $\theta = \theta_2$ and $q_L = q_{23}$.

same for any longitudinal section along the channel. Thus, the hexagonal grid used by the software does not induce numerical adverse effects such as additional head losses due to the impossibility of the hexagons to align exactly with the channel walls.

4.3 Sensitivity analysis

One of the main issues in mathematical modelling of real life phenomena is the sensitivity of the solution of the model to the variation of the model parameters. Roughly speaking, the *sensitivity analysis* highlights how large is the variation of the solution with respect to the variation of the parameters. There is a large variety of methods dedicated to sensitivity analysis; some of them perform very well (in the sense that they offer relevant results) for a class of models, but they become inadequate for other classes. A very rich literature is devoted to this subject, see [42, 43], for example, for a comprehensive view of the sensitivity analysis concepts and methods.

Regarding the vegetated Saint-Venant model, we consider the water-soil α_s (as in the Darcy-Weisbach law) and the water-plant α_p friction coefficients as the parameters of the model. The porosity $\theta(\mathbf{x})$ and the altitude $z(\mathbf{x})$ functions identify a physical configuration and are considered to be time independent. The dependence of the hydro-dynamical variables on the physical configuration is obvious and will not be the subject of sensitivity analysis; it is rather a problem of ability of the vegetated Saint-Venant model and numerical ASTERIX software to offer a reliable solution

to a given hydrological problem. We note that our analysis is only a sketch, a systematic analysis being beyond the scope this article.

Sensitivity with respect to the discharge q , porosity θ_v and slope m

We proceed and make a theoretical analysis for the response of the averaged water depth value along the vegetated zone $9 \leq x \leq 18$ to the variation of the environmental variables q , θ_v and m . Let us introduce $\bar{h}((\alpha_s, \alpha_p); (q, \theta_v, m))$ by

$$\bar{h}((\alpha_s, \alpha_p); (q, \theta_v, m)) := \frac{1}{N_v} \sum_i h(x_i; (\alpha_s, \alpha_p); (q, \theta_v, m)), \quad (27)$$

where N_v is the number of grid points $x_i \geq 9$ taken inside the vegetated zone, $h(x_i; (\alpha_s, \alpha_p); (q, \theta_v, m))$ is the steady water depth value given by the numerical model evaluated at x_i with the following environmental variables: discharge $q_L = q$, the porosity θ_v and the slope m . One defines a regular grid inside the local domain Λ :

$$\alpha_s^i = \underline{\alpha_s} + (i - 1)\Delta_s, \quad \alpha_p^j = \underline{\alpha_p} + (j - 1)\Delta_p,$$

for $i = \overline{1, N_s}$ and $j = \overline{1, N_p}$. The sensitivity is quantified by:

$$\begin{aligned} \delta_s \bar{h}(\mathbf{p}) &:= \frac{1}{(N_s - 1)N_p} \sum_{i=1}^{N_s-1} \sum_{j=1}^{N_p} \frac{\bar{h}((\alpha_s^{i+1}, \alpha_p^j); \mathbf{p}) - \bar{h}((\alpha_s^i, \alpha_p^j); \mathbf{p})}{\Delta_s}, \\ \delta_p \bar{h}(\mathbf{p}) &:= \frac{1}{N_s(N_p - 1)} \sum_{i=1}^{N_s} \sum_{j=1}^{N_p-1} \frac{\bar{h}((\alpha_s^i, \alpha_p^{j+1}); \mathbf{p}) - \bar{h}((\alpha_s^i, \alpha_p^j); \mathbf{p})}{\Delta_p}, \end{aligned} \quad (28)$$

where \mathbf{p} stands for the environmental variables $\mathbf{p} = (q, \theta_v, m)$. The two values of these functions δ_s and δ_p for a given environmental variable \mathbf{p} represent some average measures of the variation of the water depth \bar{h} defined in (27) with respect to the water-soil α_s and water-plant α_p friction coefficients, respectively.

Fig. 16 illustrates the behavior of the sensitivities δ_s (top row) and δ_p (bottom row) of the model with respect to the environmental variables \mathbf{p} . The porosity θ is fixed to $\theta_v = 0.9936$ on the first column and the slope m is fixed to the

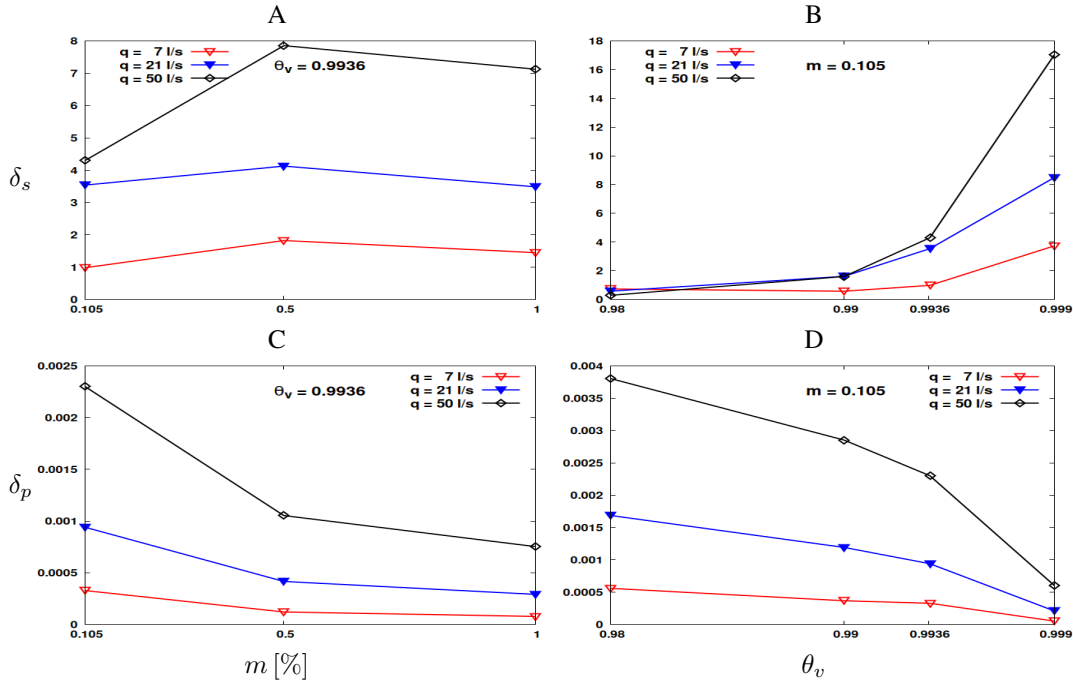


Figure 16: Sensitivities δ_s (top row) and δ_p (bottom row) of the model with respect to the environmental variables $\mathbf{p} = (q, \theta_v, m)$. The values of the sensitivities on the first column are calculated with constant porosity θ_v . The values of the sensitivities on the second column are calculated with constant slope m .

value 0.105 on the second column. A first observation we can make is that, in general, the sensitivity increases with the discharge q . An exception can be noticed for δ_s at small values of θ_v , see the picture B. As expected, a lower vegetation density leads to higher sensitivity with respect to the water-soil friction coefficient and lower sensitivity with respect to the water-plant friction coefficient, see pictures B and D. Also, as the longitudinal slope m increases (the gravitational forces start to dominate), the sensitivity with respect to the water-plant friction coefficient diminishes, see picture C. We can also observe that the sensitivity with respect to the water-soil friction coefficient increases for small values of m and decreases for higher values of m , see picture A.

Estimation of friction coefficients

Parameter estimation of a physical model is of crucial importance to ensure the accuracy of the model. The choice of an algorithm for solving this problem depends on the model and the available observational data. For example, in [44], the authors propose an automatic calibration method to estimate some parameters in a fully distributed shallow water equation system. The method is based on the Gauss-Marquardt-Levenberg algorithm to minimize a cost function and assumes the evaluation of the first and second order derivatives of the objective function. Since the analytic evaluation is almost impossible, a discrete derivative evaluation must be developed. Here is the place where the sensitivity of the model with respect to parameters comes into play.

The parameters α_s and α_p can not be directly measured, they must be estimated by other methods. Therefore, it is very important to know how its imprecise assessment affects the solution of the Saint-Venant equation. To find these parameters, we use here an inverse method and the measurements of an experiment reported in [22].

To illustrate the difficulties of estimating these friction parameters, we minimize the errors between the measured and calculated water depth on a 21×26 grid inside the domain

$$\Lambda := \{(\alpha_s, \alpha_p) \mid 0.0025 \leq \alpha_s \leq 0.0185, 55 \leq \alpha_p \leq 80\}.$$

In this sense, we define the error function

$$\chi(\alpha_s, \alpha_p) := \sqrt{\frac{1}{N_e N_g} \sum_{l=1}^{N_e} \sum_{i=1}^{N_g} (h^{\text{exp}}(x_i^l) - h(x_i^l; \alpha_s, \alpha_p))^2},$$

where N_e is the number of considered experiments, N_g is the number of gauges placed inside the channel for measurements, x_i^l is the position of the gauge G_i on the l^{th} experiment, while h^{exp} and h are the measured and calculated water depths, respectively. For example, if all six experiments (with $N_g = 17$ gauges) reported in [22] are used, then the error takes the following form:

$$\chi(\alpha_s, \alpha_p) = \sqrt{\frac{1}{102} \sum_{j,k,i} (h^{\text{exp}}(x_i^k; q_{jk}; \theta_k) - h(x_i^k; q_{jk}; \theta_k, \alpha_s, \alpha_p))^2}. \quad (29)$$

with

$$j = \overline{1, 3}, \quad k = \overline{1, 2}, \quad i = \overline{1, 17},$$

and

$$\begin{aligned} q_{11} &= 71/\text{s}, & q_{21} &= 151/\text{s}, & q_{31} &= 211/\text{s}, \\ q_{12} &= 71/\text{s}, & q_{22} &= 151/\text{s}, & q_{32} &= 501/\text{s}. \end{aligned}$$

For solving a minimization problem, we use the ‘‘Optimization by pattern search’’ algorithm [45] based on the ‘‘Direct Search’’ method introduced in [46]. We consider the following cases:

Case I: Experiment with $\theta = \theta_1, q = q_{21}$;

Case II: Experiments with $\theta = \theta_1, q \in \{q_{11}, q_{21}, q_{31}\}$;

Case III: Experiments with $\theta = \theta_2, q \in \{q_{12}, q_{22}, q_{32}\}$;

Case IV: All six experiments: $\theta = \theta_1, q \in \{q_{11}, q_{21}, q_{31}\}$ and $\theta = \theta_2, q \in \{q_{12}, q_{22}, q_{32}\}$.

When using only one experiment, e.g. **Case I**, the minimum is poorly located: there are many pairs (α_s, α_p) in the area of minimum error and it is not possible to decide which one is the best. For **Case II** and **Case III**, each with 3 experiments, the parameters are not yet sufficiently well located: α_s is poorly located in **Case II** and α_p is poorly located in **Case III**. For **Case IV**, the surface of the error function (29) is drawn in Fig. 17 and the minimum is the better located:

$$\alpha_s = 0.00709 \quad \text{and} \quad \alpha_p = 73.39. \quad (30)$$

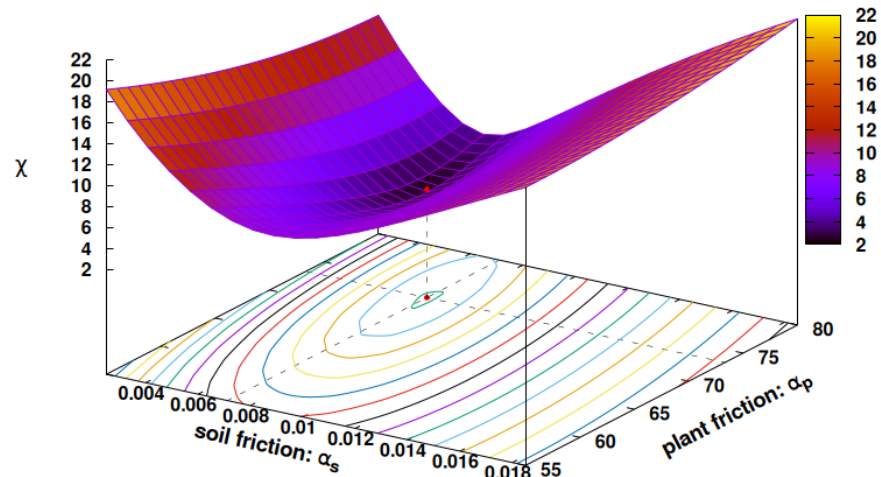


Figure 17: The error surface for Case IV. The minimum of this function is reached at $\alpha_s = 0.00709$, $\alpha_p = 73.39$:
 $\min = \chi(0.00709, 73.39) = 2.26$ mm.

5 Conclusions and final remarks

This paper describes a new module of ASTERIX dedicated to compute the solution of Saint-Venant equations in the presence of vegetation for water flow modelling. Based on a first-order numerical scheme, the computational effort is reasonable and this makes it suitable to be used from laboratory level up to practical applications for environmental problems where the flow surface can be quite large.

The software is designed to work on regular spatial hexagonal network. The software provides a “porting data” module [23] for generating a hexagonal raster by using data from a rectangular raster or analytical functions. The hexagonal raster can also be used for purposes other than supporting grid for numerical scheme, e.g flow routing or cellular automata. The core of the software consists of two modules: porting data numerical integration. Both modules were designed based on two principles: as simple and as “universal” as possible. By universal we mean that the software can be used for a large class of physical environments: topography, land use, hydrographic basins, soil physics, meteorology, etc. We keep it simple in order to allow one to add new modules to cope with given specific conditions or requirements, e.g. boundary conditions varying in time and space, distributed parameters or a post-processing data module. The source code and the user manual contain many details to facilitate the modification of the existent functions or to introduce new ones. The user are free to do all he/she wishes.

A lot of work was spent to create a video interface that allows the visualization of the evolution of the hydrodynamic variables over time. This facility can be informative for hydrologist or environmental policymaker.

Another purpose of the software is to be used as a part of an inverse method designed to estimate some physical parameters of the mathematical model. In this sense, the numerical integration module has been planned to run independently from the other modules. The Subsection 4.3 presents an example of an inverse method to estimate the coefficients α_s and α_p based on a laboratory experiment. Unfortunately, the problem of parameter estimation by an inverse method is ill-posed in the sense that very poor localization of minimal point of the cost function or amplification of the error in data are reached. For example, we found that both parameters α_s and α_p are very poorly located when the functional cost is built up on a single experiment, but they are very well located when one use more and different experiments (Case IV).

It should be noted that, in addition to the distribution of the plant cover, the configuration of the soil surface and the water discharge for which the measurements are made are important for the determination of α_s and α_p . This is also highlighted by the theoretical investigation of the sensitivity of the model with respect to q , θ_v and m from the second part of Subsection 4.3, as can also be noted from Fig. 16.

We can also imagine other scenarios (with variable θ or different values of the slope m , for example), but we did not go further because we wanted to remain inside the frame of experimental measurements. This investigation suggests that one must cleverly choose a set of experiments with different configurations in order to determine the parameters as best as possible.

In real conditions, the terrain is heterogeneous and working only with a single value for α_s and a single value for α_p can be risky and therefore, distributed values on the entire domain should be used instead. In such cases, a possible solution is to partition the surface into quasi-homogeneous subdomains with constant friction parameters.

The estimation of the porosity function is an important issue from a real application point of view. For the case of well structured cover plant (agricultural land, forest or laboratory experiment), one can easily estimate the area of domain occupied by the plant stems, but for other cases this estimation is very difficult. A possible solution to this problem is to combine the terrain pointwise determination with LiDAR measurements or aerial photography. Another solution is to set up an inverse method to find the porosity function.

Future Extensions

- ASTERIX does not yet take into account the water infiltration and interception, but an extension in this sense is in progress. For example, adapting the mass sources \mathfrak{M} through algebraic type laws can be a solution to include these processes.
- A module for the erosion and sedimentation processes based on the Hairsine-Rose model [47, 48, 49] is being prepared to be attached to our software in the near future.
- Some spatial distributed quantities are only available as scattered data affected or not by noise. In this sense, we are also considering implementing a module for treating and porting such data on hexagonal raster.

CRedit authorship contribution statement

All three authors contributed equally to this work: Conceptualization, Methodology, Software, Validation, Formal analysis, Data Curation, Writing - Original Draft.

Declaration of competing interest

The authors declare that they have no known competing financial interests or personal relationships that could have appeared to influence the work reported in this paper.

Appendices

A Details on the Numerical Scheme

The numerical scheme (16) is the result of combining the following systems from [20]

$$\sigma_i(\theta_i h_i)^* = \sigma_i(\theta_i h_i)^n + \Delta t_n \mathcal{L}_i((h, \mathbf{v})^n), \quad (31a)$$

$$\sigma_i(\theta_i h_i v_{a i})^* = \sigma_i(\theta_i h_i v_{a i})^n + \Delta t_n \mathcal{J}_{a i}^v((h, \mathbf{v})^n) + \Delta t_n \mathcal{S}_{a i}((h, w)^n), \quad (31b)$$

$$\sigma_i(\theta_i h_i)^{n+1} = \sigma_i(\theta_i h_i)^* + \sigma_i \Delta t_n \mathfrak{M}_i(t^{n+1}, h^{n+1}), \quad (32a)$$

$$\sigma_i(\theta_i h_i v_{a i})^{n+1} = \sigma_i(\theta_i h_i v_{a i})^* - \Delta t_n \mathcal{K}_i(h^{n+1}) |\mathbf{v}_i^{n+1}| v_{a i}^{n+1}. \quad (32b)$$

with $a = 1, 2$. To get the solution of (16), one must solve

- the scalar nonlinear equation for h_i^{n+1} obtained by combining (31a) and (32a), and
- the 2D nonlinear system of equations for velocity \mathbf{v}_i^{n+1} obtained by combining (31b) and (32b).

Solving (16) is accomplished in three steps:

1. Set Δt_n subject to the restriction

$$\Delta t_n < \tau_n,$$

where

$$\tau_n = CFL \frac{\phi_{\min}}{c_{\max}^n}, \quad (33)$$

with

$$c_i = |\mathbf{v}|_i + \sqrt{gh_i}, \quad c_{\max} = \max_i \{c_i\},$$

$$\phi_{\min} = \min_i \left\{ \frac{\sigma_i}{\sum_{j \in \mathcal{N}(i)} l_{(i,j)}} \right\}. \quad (34)$$

2. Calculate h_i^{n+1} using the mass balance relation of (16).
3. Solve the 2D nonlinear system of equations in \mathbf{v}_i^n given by linear momentum relations of (16).

The time step limitation is imposed by the hyperbolic character of the shallow-water equations and by the positivity-preserving requirement of the water depth. CFL is a number between 0 and 1 (the Courant-Friedrichs-Lewy condition). The reader is referred to Appendix A for extended details on the last two steps.

When the software is used to study the Riemann Problem or models that develop shock type discontinuity, it is recommended [35, 50] to use an augmented linear momentum flux $\mathcal{J}_{a i}^v$ instead of $\mathcal{J}_{a i}(h, \mathbf{v})$:

$$\mathcal{J}_{a i}^v := \mathcal{J}_{a i}(h, \mathbf{v}) + \sum_{j \in \mathcal{N}(i)} l_{(i,j)} \nu_{a(i,j)}(h, \mathbf{v}). \quad (35)$$

This update is based on the artificial viscosity

$$\nu_{a(i,j)}(h, \mathbf{v}) := c_{(i,j)} \mu_{(i,j)} ((v_a)_j - (v_a)_i), \quad (36)$$

where

$$c_{(i,j)} = \max\{c_i, c_j\}, \quad \mu_{(i,j)} = \frac{2\theta_i h_i \theta_j h_j}{\theta_i h_i + \theta_j h_j}. \quad (37)$$

This last step has an analytic solution of the form

$$\mathbf{v}_i^{n+1} = \mu \cdot (\theta_i h_i \mathbf{v}_i)^*, \quad (38)$$

where

$$\mu = \frac{2}{\alpha + \sqrt{\alpha^2 + 4\beta|\gamma|}}, \quad (39)$$

with

$$\alpha := (\theta_i h_i)^{n+1}, \quad \beta := \Delta t_n \mathcal{K}(h_i^{n+1}, \theta_i), \quad \gamma_a := (\theta_i h_i v_{a i})^*.$$

Note that for the particular cases when the mass source \mathfrak{M} does not depend on h (e.g. only the rain is taken into consideration), the computation of h_i^{n+1} is direct and does no longer require to solve a nonlinear equation.

B Analytic Solution for Thacker's Problem

We present here a particular analytic solution of the shallow-water equations (1) in the absence of vegetation ($\theta = 1$), for $t^p = \mathbf{0}$ and $t^s = h\tau\mathbf{v}$, where τ is a proportionality coefficient, for a soil surface $z(\mathbf{x})$ of the form

$$z(x, y) = a(x - x_0)^2 + b(y - y_0)^2, \quad a, b > 0, \quad (40)$$

and for a water velocity which does not depend on space variable, i.e. $\mathbf{v}(t, \mathbf{x}) = \mathbf{f}(t)$. To avoid confusions in formulas, we consider

$$\mathbf{x} = (x, y)^T \quad \text{and} \quad \mathbf{v} = (u, v). \quad (41)$$

A damped non-oscillating solution is obtained if

$$\Delta_a := \tau^2 - 8ga > 0 \quad \text{and} \quad \Delta_b := \tau^2 - 8gb > 0. \quad (42)$$

In order to write the general solution of the flow, we introduce the notations:

$$u_0 := u(0), \quad u'_0 := u'(0), \quad v_0 := v(0), \quad v'_0 := v'(0), \quad (43)$$

$$\lambda_1 = \lambda_1^\Delta := \frac{-\tau - \sqrt{\Delta}}{2}, \quad \lambda_2 = \lambda_2^\Delta := \frac{-\tau + \sqrt{\Delta}}{2}, \quad (44)$$

$$A = A^\Delta := \frac{V_0 \lambda_2 - V'_0}{\sqrt{\Delta}}, \quad B = B^\Delta := -\frac{V_0 \lambda_1 - V'_0}{\sqrt{\Delta}}, \quad (45)$$

$$V(t; \Delta, V_0, V'_0) := Ae^{\lambda_1 t} + Be^{\lambda_2 t}, \quad (46)$$

$$W_0(t; \Delta, V_0, V'_0) := \frac{1}{2g} \left[A^2 \frac{\lambda_2}{\lambda_1} (1 - e^{2\lambda_1 t}) + B^2 \frac{\lambda_1}{\lambda_2} (1 - e^{2\lambda_2 t}) + 2AB (1 - e^{-\tau t}) \right], \quad (47)$$

$$w_0(t) := w_0(t; \Delta_a, \Delta_b, u_0, v_0, u'_0, v'_0) := w_0 + W_0(t; \Delta_a, u_0, u'_0) + W_0(t; \Delta_b, v_0, v'_0). \quad (48)$$

The general solution can now be written as

$$\begin{cases} h(t, x, y) = [w(t, x, y) - z(x, y)]_+, \\ u(t) = V(t; \Delta_a, u_0, u'_0), \\ v(t) = V(t; \Delta_b, v_0, v'_0), \end{cases} \quad (49)$$

where $[\alpha]_+$ is the positive part of α and

$$w(t, x, y) := w_0(t) - \frac{1}{g}(x - x_0)(\tau u(t) + u'(t)) - \frac{1}{g}(y - y_0)(\tau v(t) + v'(t)) \quad (50)$$

is the evolution of the free water surface.

Note: A damped oscillating solution is obtained if both inequalities (42) are not satisfied; if only one of the inequalities is not satisfied, then the solution is oscillating only in one direction.

C Rainfall Hyetograph: triangular model

This rainfall model has three parameters: the total time T_d of the rain, the maximum intensity i_a of the rain and the time t_a at which this maximum intensity is recorded. The ratio between the total time T_d and the moment of time t_a is called the rainfall advance coefficient.

$$\gamma = \frac{t_a}{T_d}.$$

The graph of the instantaneous rain intensity $r(t)$

$$r(t) = \begin{cases} i_a \frac{t}{t_a}, & 0 \leq t \leq t_a, \\ i_a \frac{1 - t/T_d}{1 - \gamma}, & t_a < t \leq T_d, \\ 0, & \text{otherwise} \end{cases}$$

over the time interval $[0, T_d]$ has the shape of a triangle with T_d and i_a as its base and height, respectively (see Fig. 18).

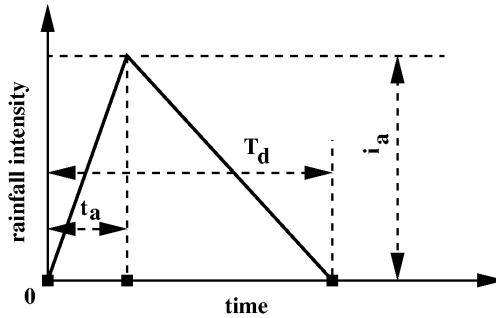


Figure 18: Hyetograph of a rainfall: triangular model.

The amount of water falling over the interval $[t_1, t_2]$ is:

$$V(t_1, t_2) = \int_{t_1}^{t_2} r(t) dt,$$

and therefore, the total amount of water falling over the interval $[0, T_d]$ is equal to the area of the triangle:

$$V = \frac{i_a T_d}{2}.$$

References

- [1] World Bank, Water resources management (2022).
URL <https://www.worldbank.org/en/topic/waterresourcesmanagement>
- [2] United Nations Environment Programme, Disasters and climate change (2024).
URL <https://www.unep.org/topics/fresh-water/disasters-and-climate-change>
- [3] OECD, Toolkit for Water Policies and Governance, OECD Publishing, Paris, 2021. doi:10.1787/ed1a7936-en.
URL <https://www.oecd-ilibrary.org/content/publication/ed1a7936-en>
- [4] D.-H. Kim, J. M. Johnson, K. C. Clarke, H. K. McMillan, Untangling the impacts of land cover representation and resampling in distributed hydrological model predictions, *Environmental Modelling & Software* 172 (2024) 105893. doi:10.1016/j.envsoft.2023.105893.
- [5] Y. Zhou, Y. Zhang, J. Vaze, P. Lane, S. Xu, Improving runoff estimates using remote sensing vegetation data for bushfire impacted catchments, *Agricultural and Forest Meteorology* 182-183 (2013) 332–341. doi:10.1016/j.agrformet.2013.04.018.
- [6] R. Orth, M. Staudinger, S. I. Seneviratne, J. Seibert, M. Zappa, Does model performance improve with complexity? A case study with three hydrological models, *Journal of Hydrology* 523 (2015) 147–159. doi:10.1016/j.jhydrol.2015.01.044.
- [7] G. Schoups, N. C. van de Giesen, H. H. G. Savenije, Model complexity control for hydrologic prediction, *Water Resources Research* 44 (12) (2008) W00B03, 1–14. doi:10.1029/2008WR006836.
- [8] K. Beven, A manifesto for the equifinality thesis, *Journal of Hydrology* 320 (1) (2006) 18–36, the model parameter estimation experiment. doi:10.1016/j.jhydrol.2005.07.007.
- [9] H. Wheater, S. Sorooshian, K. D. Sharma, *Hydrological Modelling in Arid and Semi-Arid Areas*, Cambridge University Press, 2007. doi:10.1017/CB09780511535734.
- [10] J. Sitterson, C. Knightes, R. Parmar, K. Wolfe, M. Muche, B. Avant, An overview of rainfall-runoff model types, Tech. rep., U.S. Environmental Protection Agency, USA (2017).
- [11] I. P. Sam Albers, Cran task view: Hydrological data and modeling (2024).
URL <https://CRAN.R-project.org/view=Hydrology>
- [12] R. Collenteur, Python hydrology tools (2024).
URL <https://github.com/raoulcollenteur/Python-Hydrology-Tools>
- [13] C. Brendel, R. Capell, A. Bartosova, Rational gaze: Presenting the open-source HYPETools R package for analysis, visualization, and interpretation of hydrological models and datasets, *Environmental Modelling & Software* 178 (2024) 106094. doi:10.1016/j.envsoft.2024.106094.
- [14] M. Abbott, J. Bathurst, J. Cunge, P. O’Connell, J. Rasmussen, An introduction to the european hydrological system — système hydrologique européen, “she”, 1: History and philosophy of a physically-based, distributed modelling system, *Journal of Hydrology* 87 (1) (1986) 45–59. doi:10.1016/0022-1694(86)90114-9.
- [15] DHI, Mike she (2024).
URL <https://www.dhigroup.com/technologies/mikepoweredbydhi/mike-she>
- [16] D. Woolhiser, R. Smith, D. Goodrich, U. A. R. Service, KINEROS: A Kinematic Runoff and Erosion Model: Documentation and User Manual, 1 disc with report, U.S. Department of Agriculture, Agricultural Research Service, ARS-77, 1989.
- [17] X. Liang, D. P. Lettenmaier, E. F. Wood, S. J. Burges, A simple hydrologically based model of land surface water and energy fluxes for general circulation models, *Journal of Geophysical Research: Atmospheres* 99 (D7) (1994) 14415–14428. doi:10.1029/94JD00483.
- [18] V. P. Singh, *Computer Models of Watershed Hydrology*, Water Resources Publications, LCC, 2012.
URL <https://www.wrpllc.com/books/cmwhn.html>
- [19] O. Delestre, C. Lucas, P.-A. Ksinant, F. Darboux, C. Laguerre, et al., SWASHES: a compilation of shallow water analyticsolutions for hydraulic and environmental studies, *International Journal for Numerical Methods in Fluids* 72 (3) (2013) 269–300. doi:10.1002/fld.3741.
- [20] S. Ion, D. Marinescu, S. G. Cruceanu, Numerical scheme for solving a porous Saint-Venant type model for water flow on vegetated hillslopes, *Appl. Numer. Math.* 172 (2022) 67–98. doi:10.1016/j.apnum.2021.09.019.

- [21] J. Hiver, Adverse-Slope and Slope (Bump), in: S. Soares-Frazão, M. Morris, Y. Zech (Eds.), *Concerted Action on Dam Break Modelling - CADAM: Objectives, Project Report, Test Cases, Meeting Proceedings*, Université Catholique de Louvain, Civ. Eng. Dept., Hydraulic Division, Louvain-la-Neuve, Belgium (CD-ROM), 2000, Report SR 571 HR Wallingford.
- [22] V. Dupuis, S. Proust, C. Berni, A. Paquier, Combined effects of bed friction and emergent cylinder drag in open channel flow, *Environmental Fluid Mechanics* 16 (6) (2016) 1173–1193. doi:10.1007/s10652-016-9471-2.
- [23] S. Ion, D. Marinescu, S. G. Cruceanu, V. Iordache, A data porting tool for coupling models with different discretization needs, *Environmental Modelling & Software* 62 (2014) 240–252. doi:10.1016/j.envsoft.2014.09.012.
- [24] H. Rouse, *Elementary Mechanics of Fluids Hardcover*, John Wiley and Sons, Inc., New York, USA, 1946.
- [25] M. J. Baptist, V. Babovic, J. R. Uthurburu, M. Keijzer, R. E. Uittenbogaard, A. Mynett, A. Verwey, On inducing equations for vegetation resistance, *Journal of Hydraulic Research* 45 (4) (2007) 435–450. doi:10.1080/00221686.2007.9521778.
- [26] H. M. Nepf, Drag, turbulence, and diffusion in flow through emergent vegetation, *Water Resources Research* 35 (2) (1999) 479–489. doi:10.1029/1998WR900069.
- [27] S. Whitaker, Diffusion and dispersion in porous media, *AIChE Journal* 13 (3) (1967) 420–427. doi:10.1002/aic.690130308.
- [28] K. Guo, M. Guan, D. Yu, Urban surface water flood modelling - a comprehensive review of current models and future challenges, *Hydrology and Earth System Sciences* 25 (5) (2021) 2843–2860. doi:10.5194/hess-25-2843-2021.
- [29] B. F. Sanders, J. E. Schubert, H. A. Gallegos, Integral formulation of shallow-water equations with anisotropic porosity for urban flood modeling, *Journal of Hydrology* 362 (1-2) (2008) 19–38. doi:10.1016/j.jhydrol.2008.08.009.
- [30] V. Guinot, B. F. Sanders, J. E. Schubert, Dual integral porosity shallow water model for urban flood modelling, *Advances in Water Resources* 103 (2017) 16–31.
- [31] S. Soares-Frazão, F. Franzini, J. Linkens, J.-C. Snaps, Investigation of distributed-porosity fields for urban flood modelling using single-porosity models, *E3S Web of Conferences* 40 (2018) 06040. doi:10.1051/e3sconf/20184006040.
- [32] G. Varra, L. Cozzolino, R. Della Morte, S. Soares-Frazão, Shallow water equations with binary porosity and their application to urban flooding, *Physics of Fluids* 36 (7). doi:10.1063/5.0214441.
- [33] G. Strang, On the construction and comparison of difference schemes, *SIAM Journal on Numerical Analysis* 5 (3) (1968) 506–517. doi:10.1137/0705041.
- [34] R. J. LeVeque, *Time-split methods for partial differential equations*, Ph.D. thesis, Stanford University, Stanford, California, USA (1982).
- [35] R. J. LeVeque, *Finite Volume Methods for Hyperbolic Problems*, Cambridge Texts in Applied Mathematics, Cambridge University Press, Cambridge, UK, 2002. doi:10.1017/CB09780511791253.
- [36] S. Ion, D. Marinescu, S. Cruceanu, Analysis of the effects of curvature on the solutions of shallow water equations, in: *2023 13th International Symposium on Advanced Topics in Electrical Engineering (ATEE)*, 2023, pp. 1–6. doi:10.1109/ATEE58038.2023.10108117.
- [37] W. Thacker, Some exact solutions to the nonlinear shallow-water equations, *Journal of Fluid Mechanics* 107 (1981) 499–508. doi:10.1017/S0022112081001882.
- [38] J. J. Sampson, A. Easton, M. Singh, Moving boundary shallow water flow in a region with quadratic bathymetry, *ANZIAM Journal* 49 (2007) C666–C680. doi:10.21914/anziamj.v49i0.306.
- [39] N. Matskevich, L. Chubarov, Exact solutions to shallow water equations for a water oscillation problem in an idealized basin and their use in verifying some numerical algorithms, *Numerical Analysis and Applications* 12 (2019) 234–250. doi:10.1134/S1995423919030030.
- [40] S. Ion, D. Marinescu, S.-G. Cruceanu, Constructive approach of the solution of the Riemann problem for shallow water equations with topography and vegetation, *An. St. Univ. Ovidius* 28 (2) (2020) 93–114. doi:10.2478/auom-2020-0021.
- [41] Google Earth, Map of Șușița river basin (2024).
 URL <https://earth.google.com/web/@45.94352578,26.99150326,231.35063202a,61462.69767313d,35y,0h,0t,0r/data=OgMKATA>

- [42] A. Saltelli, K. Chan, E. Scott, *Sensitivity Analysis*, Wiley, 2009.
- [43] A. Saltelli, K. Aleksankina, W. Becker, P. Fennell, F. Ferretti, N. Holst, S. Li, Q. Wu, Why so many published sensitivity analyses are false: A systematic review of sensitivity analysis practices, *Environmental Modelling & Software* 114 (2019) 29–39. doi:10.1016/j.envsoft.2019.01.012.
- [44] G. García-Alén, C. Montalvo, L. Cea, J. Puertas, Iber-PEST: Automatic calibration in fully distributed hydrological models based on the 2D shallow water equations, *Environmental Modelling & Software* 177 (2024) 106047. doi:10.1016/j.envsoft.2024.106047.
- [45] Y. S. Sherif, B. A. Boice, Optimization by pattern search, *European Journal of Operational Research* 78 (3) (1994) 277–303. doi:10.1016/0377-2217(94)90041-8.
- [46] R. Hooke, T. A. Jeeves, “direct search” solution of numerical and statistical problems, *Journal of the ACM* 8 (2) (1961) 212–229. doi:10.1145/321062.321069.
- [47] P. Hairsine, C. Rose, Modeling water erosion due to overland flow using physical principles: 1. sheet flow, *Water Resources Research* 28 (1) (1992) 237–243. doi:10.1029/91WR02380.
- [48] J. Kim, V. Y. Ivanov, N. D. Katopodes, Modeling erosion and sedimentation coupled with hydrological and overland flow processes at the watershed scale, *Water Resources Research* 49 (9) (2013) 5134–5154. doi:10.1002/wrcr.20373.
- [49] G. Sander, J.-Y. Parlange, D. Barry, M. Parlange, W. L. Hogarth, Limitation of the transport capacity approach in sediment transport modeling, *Water Resources Research* 43 (2), w02403. doi:10.1029/2006WR005177.
- [50] A. Kurganov, G. Petrova, A second-order well-balanced positivity preserving central-upwind scheme for the Saint-Venant system, *Communications in Mathematical Sciences* 5 (1) (2007) 133–160. doi:10.4310/CMS.2007.v5.n1.a6.